



HAL
open science

Kinematics of the Kahramanmaraş triple junction: evidence of shear partitioning

Volkan Özbey, A. M. Celâl Şengör, Pierre Henry, M. Sinan Özeren, Elliot C. Klein, A. John Haines, Ergin Tari, Cengiz Zabci, Konstantinos Chousianitis, Sezim E. Güvercin, et al.

► **To cite this version:**

Volkan Özbey, A. M. Celâl Şengör, Pierre Henry, M. Sinan Özeren, Elliot C. Klein, et al.. Kinematics of the Kahramanmaraş triple junction: evidence of shear partitioning. 2023. hal-04053058v1

HAL Id: hal-04053058

<https://hal.science/hal-04053058v1>

Preprint submitted on 31 Mar 2023 (v1), last revised 13 Oct 2023 (v2)

HAL is a multi-disciplinary open access archive for the deposit and dissemination of scientific research documents, whether they are published or not. The documents may come from teaching and research institutions in France or abroad, or from public or private research centers.

L'archive ouverte pluridisciplinaire **HAL**, est destinée au dépôt et à la diffusion de documents scientifiques de niveau recherche, publiés ou non, émanant des établissements d'enseignement et de recherche français ou étrangers, des laboratoires publics ou privés.

Tectonophysics

Kinematics of the Kahramanmaraş triple junction: evidence of shear partitioning

--Manuscript Draft--

Manuscript Number:	TECTO16305
Article Type:	Research Paper
Keywords:	Deformation in plate boundary zones; Kahramanmaraş triple junction; Cyprus Arc; East Anatolian Fault; Kinematic Modeling
Corresponding Author:	Volkan Özbey Istanbul Technical University TURKEY
First Author:	Volkan Özbey
Order of Authors:	Volkan Özbey Celal Şengör, Dr. Pierre Henry, Dr. Mehmet Sinan Özeren, Dr. Elliot C. Klein, Dr. Alan John Haines, Dr. Ergin Tari, Dr. Cengiz Zabcı, Dr. Konstantinos Chousianitis, Dr. Sezim Ezgi Guvercin, Dr. Nazik Ogretmen, Dr.
Abstract:	<p>We present an up-to-date velocity field around the north of the eastern Mediterranean, southern Turkey, Cyprus, Levant, and East Anatolian faults therein and discuss its tectonic implications. We perform a block model inversion to calculate rigid block motion, slip rates on the dislocation sources along block boundaries. Our best fitting model locates the Sinai-Anatolia Euler pole at $32.04 \pm 1.8^\circ$ N, $38.21 \pm 2.4^\circ$ E with a 0.596 ± 0.084 clockwise rotation rate. Convergence rate on the Cyprus arc is ~ 3-6 mm/yr, progressively decreasing from west to east. Kyrenia range has a left lateral slip behavior with a 3-4 mm/yr rate. We thus show that there is shear partitioning between the Cyprus subduction and Kyrenia fault zone. The northeast prolongation of the Kyrenia fault east of the Adana basin accommodates extensional and strike-slip motion, which is consistent with focal mechanisms. Further East, the relative strike-slip motion between Arabia and Anatolia is partitioned between the East Anatolian Fault (slip rates 5-6 mm/yr) and the Çardak and Malatya faults (slip rates 1.7-1.8 mm/yr), and also causes distributed deformation between these two fault systems. The Levant fault has a 3.2-4.0 mm/yr left-lateral slip rate, decreasing northward. A continuum kinematic model shows a compressional to transpressional strain accumulation across the Cyprus arc that is also compatible with its progressive change of orientation. The largest values for the second invariant of strain rate tensor define a region from Hatay to Malatya corresponding to a 50-60 km wide East Anatolian shear zone. The whole area north of the Kahramanmaraş triple junction appear to be under E-W extension. Strain rates appear relatively small in the Taurus and vary from extensional to compressional along the mountain range.</p>
Suggested Reviewers:	Robert Reilinger rreilinger@hotmail.com Richard Walker richard.walker@earth.ox.ac.uk Leigh Royden lhroyden@mit.edu

Kinematics of the Kahramanmaraş triple junction: evidence of shear partitioning

Volkan Özbey^{1,2,*}, Ali Mehmet Celâl Şengör^{3,4}, Pierre Henry², Mehmet Sinan Özeren⁵, Elliot C. Klein⁶, A. John Haines⁷, Ergin Tari¹, Cengiz Zabcı³, Konstantinos Chousianitis⁸, Sezim Ezgi Güvercin⁹, Nazik Öğretmen⁵

Abstract

We present an up-to-date velocity field around the north of the eastern Mediterranean, southern Turkey, Cyprus, Levant, and East Anatolian faults therein and discuss its tectonic implications. We perform a block model inversion to calculate rigid block motion, slip rates on the dislocation sources along block boundaries. Our best fitting model locates the Sinai-Anatolia Euler pole at $32.04 \pm 1.8^\circ\text{N}$, $38.21 \pm 2.4^\circ\text{E}$ with a 0.596 ± 0.084 clockwise rotation rate. Convergence rate on the Cyprus arc is $\sim 3\text{-}6$ mm/yr, progressively

*Corresponding author

Email address: ozbeyv@itu.edu.tr (Volkan Özbey)

¹Istanbul Technical University, Department of Geomatics Engineering, 34469, Maslak, Istanbul, Turkey

²Aix-Marseille Universite, CNRS, IRD, INRA, Coll France, CEREGE, Aix-en-Provence, France

³Istanbul Technical University, Department of Geology, 34469, Maslak, Istanbul, Turkey

⁴Center for Global Tectonics, School of Earth Sciences, State Key Lab for Geological Processes and Mineral Resources, Badong National Observatory and Research Station for Geohazards, China University of Geosciences, Wuhan

⁵Istanbul Technical University, Eurasia Institute of Earth Sciences, 34469, Maslak, Istanbul, Turkey

⁶FM Global Research, Research Division, Norwood, MA, United States

⁷GNS Science - Institute of Geological and Nuclear Sciences, (emeritus), New Zealand

⁸Institute of Geodynamics, National Observatory of Athens, Lofos Nymfon, Athens, Greece

⁹Yıldız Technical University, Department of Geomatics Engineering, 34349, İstanbul, Turkey

decreasing from west to east. Kyrenia range has a left lateral slip behavior with a 3-4 mm/yr rate. We thus show that there is shear partitioning between the Cyprus subduction and Kyrenia fault zone. The northeast prolongation of the Kyrenia fault east of the Adana basin accommodates extensional and strike-slip motion, which is consistent with focal mechanisms. Further East, the relative strike-slip motion between Arabia and Anatolia is partitioned between the East Anatolian Fault (slip rates 5-6 mm/yr) and the Çardak and Malatya faults (slip rates 1.7-1.8 mm/yr), and also causes distributed deformation between these two fault systems. The Levant fault has a 3.2-4.0 mm/yr left-lateral slip rate, decreasing northward. A continuum kinematic model shows a compressional to transpressional strain accumulation across the Cyprus arc that is also compatible with its progressive change of orientation. The largest values for the second invariant of strain rate tensor define a region from Hatay to Malatya corresponding to a 50-60 km wide East Anatolian shear zone. The whole area north of the Kahramanmaraş triple junction appear to be under E-W extension. Strain rates appear relatively small in the Taurus and vary from extensional to compressional along the mountain range.

Keywords: Deformation in plate boundary zones, Kahramanmaraş triple junction, Cyprus Arc, East Anatolian Fault, Kinematic Modeling

Highlights

- Block and continuum models indicate a zone of distributed deformation around Kahramanmaraş triple junction
- The Cyprus arc accommodates 3-6 mm/yr convergence rate
- New GPS observations shed some light on the shear partitioning between the Cyprus arc and Kyrenia Range
- The Kyrenia fault zone connects to the East Anatolian Shear zone where Arabia-Anatolia motion is partitioned between the East Anatolian Fault and several other faults.

1 1. Introduction

2 The purpose of this paper is to present a new interpretation of the neotectonics of the northeastern Mediterranean. The region of interest is shown in
3 Fig. 1. We are specifically interested in the deformation of southern Turkey,
4 particularly around the Kahramanmaraş triple junction, and Cyprus and the
5 effect of the motion of Cyprus on the Adana/Cilicia Basin and southernmost
6 Turkey. Our principal aim is the way in which the perturbation of the rel-
7 ative Nubia motion by the presence of Cyprus shapes the regional tectonics
8 in terms of the tectonic boundary conditions in southernmost Turkey. To
9 this end, understanding the mechanics of Adana Cilicia Basin is of utmost
10 importance. The basin and its frame have been interpreted as elements of
11 a ‘forearc’ (e.g., Aksu et al., 2005, 2021, and the extensive literature cited
12 therein; Fernández-Blanco, 2014), but it has not been made clear how, or even
13 whether, this alleged position has influenced its tectonic evolution. Burton-
14 Ferguson et al. (2005) and Aksu et al. (2021) pointed out the rôle of the
15 escape of the Anatolian block in inducing a strike-slip component onto the
16 basin evolution, but they seem to imply that it was in the form of transten-
17 sion without presenting a thorough kinematic analysis of the area, especially
18 how the long fold trains in the middle of the Adana/Cilicia Basin fit into the
19 transtension interpretation, which, actually, they do not (cf. Dewey, 2002).
20 Other recent studies concentrate on the sedimentological and stratigraphic
21 evolution of the basin without setting it into its tectonic ecology (e.g., Aksu
22 et al., 2014a,b). Fernández-Blanco et al. (2020) presented model a forearc
23 atop a subduction zone, but neither the geometry, nor the direction and
24 amount of subduction can support their model. It seems therefore clear that
25 a more thorough investigation of the region is in order.

27 **Figure1**

28 The importance of this area is not that it sits in a fore-arc position with
29 respect to the Cyprus Subduction Zone, but whether that alleged setting or
30 the influence of the independent orogenic evolution of the Central Taurus
31 ranges to the north and the subsequent escape of Central and Western Ana-
32 tolia southwestward with respect to Africa have been the decisive factors in
33 its development. Şengor et al. (1980) pointed out that the Kahramanmaraş
34 triple junction, where the Levant and the East Anatolian Faults (EAF here-
35 after) and the plate boundary extending south of Turkey, gives rise to a very
36 complex pattern of deformation in the northeastern Mediterranean because
37 of the meeting at the triple junction of two non-subductable continental

38 plates, namely Arabia and Anatolia. Şengör et al. (1985, see especially their
39 fig. 16) elaborated on that theme, but the lack of sufficient number and
40 quality of observations relating to the direction and amount of the motions
41 around the triple junction prevented them from discussing the issue further.
42 Şengör et al. (2019) later noticed, from a hint by Fuat Şaroğlu (Şaroğlu pers.
43 comm. 1990) that not one, but two triple junctions are currently active
44 in the area, namely those of Kahramanmaraş and Hatay (Fig. 2) making
45 the tectonics of the region even more complicated than previously believed.
46 Triple junctions involving non-subductable plates have more than just local
47 significance. During the final phases of continental collisions, the colliding
48 continental plates often fall apart and the resulting pieces tend to move
49 with different velocities with respect to one another (e.g., McKenzie, 1972;
50 Roman, 1973; Dewey, 1977; Molnar and Tapponnier, 1975; Sengör, 1976,
51 1979; Şengör, 1995; Şengör et al., 2019). In such situations, incompatibility
52 basins such as those in the Karlıova in eastern Turkey (see especially Sengör,
53 1979; Şengör et al., 1985; Şengör et al., 2019, for an Himalayan example, see
54 Van Buer et al., 2015) and the Adana/Cilicia between Cyprus and Turkey
55 (Şengör et al., 1985; Şengör et al., 2019, for similar situations, see Ruther-
56 ford et al., 2001 for the Sumba island and Wandrey, 2004, for the much more
57 squashed Assam Basin) inevitably arise, a fact commonly not taken into ac-
58 count (e.g., Fernández-Blanco et al., 2020; Aksu et al., 2021). During the
59 advanced stages of the intracontinental shortening, many such basins do not
60 survive intact and many become severely deformed out of recognition (Fig.
61 3; for some of the Central European examples, see Şengör, 1995). Their pres-
62 ence can only be recognised if one is aware of the possibility of their presence
63 and characteristics (e.g., Van Buer et al., 2015). It is therefore of some im-
64 portance to know their characteristics for studies of the historical geology of
65 the continental convergent plate boundary zones.

66 **Figure2**

67 The northward motion of Africa, together with that of Arabia is a major
68 factor that shapes the tectonics of the Eastern Mediterranean (McKenzie,
69 1972; Sengör, 1979; Şengör et al., 1985; Şengör et al., 2019; Özeren and
70 Holt, 2010). Africa has recently been divided in the Eastern Mediterranean
71 into a Nubian and a Sinai plate or block (Mahmoud et al., 2005). The
72 relative velocities reported between them, amounting to hardly a cm/yr, are
73 insufficient to define separate plates. We use the Sinai block here, as defined
74 by Mahmoud et al. (2005), only to define a practical block geometry to be
75 able to model, albeit crudely, the current motions. Özeren and Holt (2010)

76 in their kinematic model which they used as the principal constraint for the
77 dynamical model did not use any GPS data to the south of Turkey (Because
78 there was not any except the single station, NICO, in Cyprus). This probably
79 led them to obtain, in their inversion, unrealistic stress boundary conditions
80 along the southern boundary of their study region which roughly follows the
81 southern coast of Turkey and the Hellenic Trench (fig. 7 in their study).

82 **Figure3**

83 The kinematic problem of the Eastern Mediterranean is complicated by
84 the fact that huge expanses of the region is under the Mediterranean Sea
85 and thus inaccessible to direct field observation to measure the present-day
86 motions. The only place within the Eastern Mediterranean Sea Basin, where
87 one can anchor the GPS-based kinematic deformation models is the Island of
88 Cyprus where the GPS data have been very inadequate so far, however. To
89 remedy this situation, we conducted GPS surveys in Cyprus and revisited 18
90 points that have been previously measured in 1998 and 2001. Furthermore,
91 we processed data from seven permanent GPS sites in the southern part of
92 the island. For the first time, we now have a reasonable spatial coverage of
93 space geodetic data in Cyprus enabling us to construct a kinematic model
94 of the easternmost Mediterranean alongside a more detailed understanding
95 of the deformation within Cyprus. We also revisited several GPS survey
96 sites in the Turkish mainland to constrain the kinematics from the north.
97 Furthermore, we also utilized the GPS velocities from previous studies that
98 are mentioned in detail in the relevant sections below.

99 We performed a block model approach to calculate the rigid block mo-
100 tions, and coupling on the block boundaries that are defined as dislocation
101 sources (McCaffrey et al., 2007). Our model also allows internal deformation
102 of the blocks, but the deformation within the individual blocks is not allowed
103 to vary spatially. After obtaining the slip rates, we employed a continuum
104 kinematic approach (Haines and Holt, 1993; Beavan and Haines, 2001) to
105 monitor the strain rate field of the study area. It also enables us to get a han-
106 dle on the finite strain geometry since the Miocene with a view to interpreting
107 the way in which the kinematic field may have changed spatially to the north
108 of Cyprus. This concerns the type of faulting in the Cilicia Basin and Adana
109 Basin to the northeast, which is largely buried under the thick delta deposits
110 of the rivers Seyhan (classical Saros) and Ceyhan (classical Pyramos) (e.g.
111 Aksu et al., 2014b). The proper modeling of the region using additional GPS
112 constraints is not only important for understanding the regional kinematics
113 but it is also imperative to understand the nature of the boundary condi-

114 tions imposed on Anatolia from the south. For instance, the styles of the
115 dynamically calculated strain rate tensors by England et al. (2016) just to
116 the north of the Gulf of Iskenderun show almost no compressional component
117 possibly due to the misrepresentation of the boundary forcing in the lack of
118 GPS constraints further south (see fig 9 in their manuscript; for a critique
119 of the dynamics represented in that paper, see). This has very significant
120 consequences for the deformation field in southernmost Turkey as we show
121 below. Another problem with the tectonic interpretations published so far is
122 the scant attention paid to the migration of shortening southwards from the
123 Inner Tauride suture in Turkey (see Şengör et al., 2019).

124 In the meantime, the availability and the quality of earthquake data have
125 improved dramatically and now we have a large number of fault mechanism
126 solutions and earthquake hypocentre locations. We have plotted the available
127 earthquake hypocenter data on a roughly north-south cross-section to be able
128 to see the location of the active loci of deformation. We further looked at the
129 Pleistocene and Holocene rates of uplift obtained from palaeontology. We
130 summarise all these data in the next section, before we present the new GPS
131 data with a view to combining them into a synthesis. The following section
132 reviews briefly the geological development of the area since the Oligocene,
133 which is the earliest date when the Arabian plate collided with the East Ana-
134 tolian Accretionary Complex to eliminate the Neo-Tethys in Eastern Turkey
135 and initiated the neotectonic episode in Turkey (Şengör et al., 1980; Şengör
136 et al., 1985; Şengör et al., 2003, 2008). Our review shows the relationship
137 between the events associated with the Neo-Tethyan closure along the Inner
138 Tauride Ocean and those related to the activity of the Kahramanmaraş triple
139 junction. The elucidation of that relationship is one of the main points of
140 our paper.

141 2. Regional Geology of the Study Area

142 Our area of interest forms the frame of the northeastern corner of the
143 Eastern Mediterranean and includes southern Turkey and Cyprus plus the
144 intervening marine basin of Adana/Cilicia. Fig. 4 is a geological map showing
145 only the rocks and structures younger than the Oligocene, the time interval
146 relevant to this paper. All blank areas on land are pre-Miocene rocks and
147 structures. The submarine areas are also left blank.

148 **Figure4**

149 Initially, near the end of the Oligocene, area shown in Fig. 4 was uplifted
150 and became a site of erosion or, locally, non-marine clastic deposition (Demir-
151 tasli, 1984; Özgül, 1976; Gedik et al., 1979; Ketin, 1983), in a few places dot-
152 ted with lakes that localised lacustrine sedimentation, as, for example, in the
153 case of the Ermenek Basin (İlgar and Nemeç, 2005). An irregular topography,
154 dissected by numerous river valleys of diverse sizes, was invaded by the sea
155 beginning in the Burdigalian. Widespread carbonate deposition, in places
156 laterally interfingering with clastics and passing southward into deep-water
157 turbidites, as in the Adana basin, became established with the onset of the
158 sedimentation of the so-called Silifke Formation of Middle to Upper Miocene
159 age (Gorur, 2014, 1994); correlative with it is the Tepeköy limestones, which,
160 in places, have a conglomeratic base that may reach into the Lower Miocene,
161 in places even into the uppermost Oligocene (Demirtasli, 1984; Demirtasli
162 et al., 1984; Gedik et al., 1979; Özgül, 1976; Ketin, 1983; Şafak et al., 2005;
163 Bassant et al., 2005, see the summary diagram for the entire area in Kelling
164 et al., 2005 fig. 5).

165 The sedimentation in the area shown in Fig. 4 has been interpreted in
166 terms of global sea-level changes caused by 400-Ka orbital eccentricity cycles
167 indicated by third-order sequences, and the parasequences that allegedly re-
168 sponded to 100 Ka orbital eccentricity cycles. All of this was claimed without
169 taking the local tectonics into account in a tectonically highly mobile foreland
170 environment (Bassant et al., 2005, e.g.). Miall (2010, p. 283) pointed out,
171 after a study by Naylor and Sinclair (2007), that episodicity of thrust belt
172 activity ranges between 0.1 and 5 Ma. This is of importance in interpreting
173 the sedimentary sequence development in the Göksu-Taşeli plateau, because
174 they form the upper surface of hanging wall of thrusts that have been active
175 since the early Miocene. Therefore, we find it impossible to agree with the
176 global sea-level implications claimed by Bassant et al. (2005) and ascribe the
177 facies shifts in the Mut Basin to tectonic mobility that is even more com-
178 plicated in this area than the models discussed by Miall (2010, section 10.3)
179 for the reasons discussed using Fig. 5 as a guide. Fig. 5 is a schematic rep-
180 resentation of the outlines of the Miocene tectonics of the Central Taurus.
181 Fig. 5A shows the situation before the closure of the Inner Tauride Ocean,
182 i.e., before the Bartonian. In 5B the Inner Tauride Ocean has closed by
183 the collision of the Kırşehir Block with the Menderes-Taurus Block, which
184 bent the latter in the manner shown, creating the southern ‘belly’ of Ana-
185 tolia (Şengör et al., 2019, see). The growth of the ‘belly’ was most likely
186 helped by the formation of tear fault systems represented schematically by

187 the two strike-slip lineaments as shown in Fig. 5C, now expressed mainly
188 by two prominent negative Bouger gravity anomaly lineaments, indicating
189 the presence of young sedimentary basins along them (Makris et al., 1998).
190 They are now inactive, as the shortening has already migrated south into
191 the Adana/Cilicia Basin and Cyprus. The one in the west is the Mut Basin
192 (Gedik et al., 1979; Bassant et al., 2005; Eriş et al., 2005; Şafak et al., 2005).
193 Fig. 5C shows how such a basin may have come into existence, although
194 surface evidence of faulting, in the form of steep normal faults that cut the
195 entire outcrop in the Mut Gorge, is rare, but present nevertheless. The Mut
196 Basin is here interpreted as a strike-slip related basin, although whether it
197 is a pull-apart basin, or a constraining bend flexural basin, or even a wedge
198 basin is unknown, because neither its sedimentary geometry, nor its bound-
199 ing faults have been mapped in any detail. The best existing map is that
200 by Gedik et al. (1979, fig. 2), published at a scale of 1/500,000. The dis-
201 tribution of the Burdigalian Deringay Formation on that map (see our Fig.
202 4) vaguely indicates a constraining bend basin geometry as depicted in Fig.
203 5C, but it could almost equally well be a pull-apart basin. The point here is,
204 however, that the tectonic ground motion in the Mut Basin must have been
205 a combination of the motion of a thrust fault hanging wall and strike-slip
206 basin subsidence atop it

207 **Figure5**

208 Studies on the vertical motions since the Miocene support this inter-
209 pretation. Several researchers have investigated the uplift dynamics of the
210 southern Central Anatolian Plateau in the light of a multi-phased uplift sce-
211 nario since the Miocene (Cosentino et al., 2012; Schildgen et al., 2012, 2014;
212 Cipollari et al., 2013; Radeff et al., 2017; Öğretmen et al., 2018; Racano
213 et al., 2020) involving lithospheric mantle delamination, slab roll-back and
214 break-off, and consequent asthenospheric upwelling. These studies relied on
215 cosmogenic exposure ages of gravels from the Göksu River terraces (Schildgen
216 et al., 2012), micropaleontological data from the marine deposits in Mut and
217 Adana basins (Cosentino et al., 2012; Schildgen et al., 2012; Cipollari et al.,
218 2013; Öğretmen et al., 2018), Miocene-aged fluvial conglomerates (Cosentino
219 et al., 2010; Radeff et al., 2017), and abandoned marine platforms (Racano
220 et al., 2020).

221 Cipollari et al. (2013) placed the maximum age of the surface uplift to ~ 8
222 My based on calcareous nannoplankton ages from the Mut Basin. Cosentino
223 et al. (2010) and Radeff et al. (2017) interpreted the Upper Messinian-Lower
224 Pliocene (5.45-5.33 My) fluvial conglomerate deposits of the Handere For-

225 mation (Adana Basin) as uplift-related and resulting in ~ 4 mm/yr uplift.
226 The latest uplift-phase was later revised by Öğretmen et al. (2018) through
227 detailed biostratigraphic age and paleodepth reconstructions from the Early-
228 Middle Pleistocene aged marine deposits found at ~ 1 km asl in the Mut
229 Basin pointing to ~ 3.2 - 3.4 mm/yr uplift rate since 0.46 My (Fig. 6B). Ma-
230 rine terraces developed after the deposition of these marine deposits yielded
231 similar uplift rates from 3.8-3.4 mm/yr to 1.6-1.1 mm/yr for the present-day
232 (Racano et al., 2020). Some other researchers proposed an alternative opin-
233 ion as well. For example, Fernández-Blanco et al. (2019, 2020) suggested a
234 monoclin flexural system driven by lower crustal flow resulting in forearc
235 high uplift due to Cyprus-Anatolian subduction. However, they state that
236 their model does not account for the uplift rates documented by Öğretmen
237 et al. (2018).

238 In order to understand the geometry and the cause of the vertical motions
239 in the Central Taurus, we have compiled the available earthquake data and
240 the tomographic models of the mantle beneath it. The long-term seismicity
241 catalogue between 1905 and 2019 is obtained from KOERI (KOERI:, 2001;
242 <http://www.koeri.boun.edu.tr>). The magnitude of completeness of the cat-
243 alogue is $\sim M_c=4$. The mean horizontal location uncertainty is less than 5.0
244 km in NS and E-W directions. The mean of the depth uncertainty is ~ 3.5
245 km, varying between 2.0 and 8 km. The seismicity cross-section along the
246 profile in Fig. 6B is filtered based on the quality factors such as horizontal
247 location uncertainty < 5 km and RMS < 0.5 s. For the crustal and upper
248 mantle structure, we used a cross section along a N-S profile at 34° from the
249 new high-resolution tomographic of Karabulut et al. (2019). This model is
250 computed using 860 broadband seismic stations providing an improved im-
251 age of the slab structure in the Aegean-Anatolia domain (Karabulut et al.,
252 2019). The model exhibits major discontinuities of subducting slabs from
253 Hellenic to Cyprus subduction zones.

254 Fig. 6 shows a simplified structural cross-section across Central Turkey
255 and Cyprus together with the earthquake hypocentres in the grey area where
256 the hypocentres are projected onto the profile line shown on the same fig-
257 ure. The surprising feature of this figure is the high concentration of the
258 earthquakes in the Central Taurus from where it decreases both south into
259 the Eastern Mediterranean and northward into the Ova Province of Central
260 Turkey underlain by the Kırşehir Massif (Şengör et al., 1985, for the defi-
261 nition of the ova province, see). However, as this seismic activity is of low
262 magnitude and no focal mechanisms are available we will have to rely on

263 the geodetic strain to infer the deformation style. The overall geometry is
264 strongly reminiscent of the Western and Central Alps, also shown in our Fig.
265 6A. In this scenario, the Bolkardağ Massif is the tectonic equivalent of the
266 Lepontine nappes, the Taurus Nappes of the Helvetic Nappes, the Central
267 Taurus foreland and the Cilicia Basin the equivalent of the Molasse basin
268 and the Kyrenia ranges in Cyprus the equivalent of the Jura Mountains. An
269 analogy may also be considered regarding convergence and uplift rates. Con-
270 vergence has ceased in the Western Alps and is less than 1 mm/yr along the
271 Central Alps cross section here considered (Walpersdorf et al., 2018; Serpel-
272 loni et al., 2016). Yet, uplifts rates of 1 mm/yr to 2.5 mm/yr are observed
273 in the core of the Alps and the widely accepted view is that post-glacial re-
274 bound and erosion cannot fully explain them, suggesting an involvement of
275 the mantle (Sternai et al., 2019). The possibility of a recent slab break-off
276 below the Western Alps has been proposed, but is disputed (Lippitsch et al.,
277 2003; Zhao et al., 2016). Nevertheless slab break-off is unlikely to provide a
278 satisfactory explanation for the Central Alps where a continuous lithospheric
279 slab is well imaged.

280 **Figure6**

281 Seismic tomography down-dip of the Cyprus Arc subduction shows very
282 different distributions of mantle velocity anomalies over its western part be-
283 tween Antalya and Cyprus where a slab of subducting lithosphere is indeed
284 observed to a depth of at least 300 km, and its eastern part where the slab ap-
285 pears to be interrupted. Recent studies (Portner and Hayes, 2018; Kounoudis
286 et al., 2020) confirmed cold regions in the upper mantle are under the area
287 between the Bolkar culmination, the coastal areas of Adana, Mersin and be-
288 neath the Cilicia basin. The northern edge of this zone 300 km north of
289 the subduction trench, coincides with southern edge of the Cappadocia vol-
290 canic province, where the upper mantle is anomalously hot. Below this hot
291 zone a high velocity body extends vertically in the mantle from 200-300 km
292 down to 600 km depth and has been interpreted as resulting from slab break
293 off. One may wonder if this volume of lithospheric material can be truly
294 attributed to the Cyprus Arc subduction. The total convergence between
295 Africa and Eurasia since the beginning of the Oligocene in this region is at
296 least 400 km (Rosenbaum et al., 2002) and this value does not account for
297 additional convergence due to the motion of Anatolia since about 13 Ma
298 that could amount to a maximum of about 100 km. However, part of the
299 total convergence has been accommodated by intracontinental shortening in
300 Anatolia and the initiation of subduction could have happened anytime be-

301 tween the Eocene Tauride collision and the Miocene initiation of Anatolian
302 extrusion. This leaves a large uncertainty on the amount of lithosphere sub-
303 ducted. Moreover, the limit between the western and eastern domains of
304 the Cyprus Arc also corresponds to the limit between subduction of oceanic
305 crust and subduction of thinned continental crust (Le Pichon et al., 2019)
306 and it appears likely that a vertical slab tear is present between these two do-
307 mains in the prolongation of the Paphos Fault (Guvercin et al., 2021). There
308 are thus several possibilities to explain the tomographic images. The most
309 commonly proposed interpretation is an ongoing slab break off along an hor-
310 izontal tear propagating westward (Biryol et al., 2011; Portner and Hayes,
311 2018; Kounoudis et al., 2020) and the history of magmatism suggests this
312 process may have started during the Middle Miocene from a tear between
313 the Cyprus and the Bitlis slabs (Reid et al., 2019). Another is to consider
314 that the Eastern part of the Cyprus Arc has not, or only briefly functioned
315 as an oceanic subduction. In this case, the high velocity zone observed in the
316 deeper mantle may represent continental lithosphere dropped from below the
317 Central Anatolian Plateau (Gögüş et al., 2017), combined with slabs from
318 older subductions north of the Taurus block.

319 The question now becomes, how this ‘orogenic’ model relates to the
320 present-day motions in the area. The following section utilizes the new GPS
321 data in addition to the existing data to construct two kinematic models (a
322 block model and a continuum model) to shed light on the present-day be-
323 havior of this enigmatic region.

324 **3. GPS Observations and Analysis**

325 *3.1. GPS Data*

326 The data assessment was performed with a combination of GAMIT/GLOBK
327 software Herring et al. (2018) and a stochastic approach we adopted. In order
328 to determine the coordinates of all stations for each session (day), Interna-
329 tional GNSS Service (IGS) final orbit and clock products were used. We
330 also preferred to incorporate the IGS sites into the evaluation to apply more
331 reliable constraints. This is because there were fewer permanent stations
332 before 2009. GAMIT/GLOBK software integrates the double differences
333 method and some combinations of the different carrier phases to eliminate
334 both geometric and non-dispersive delays into the solution. We also utilized
335 the VMF1 mapping function to minimize the effect of the tropospheric delay
336 (Boehm et al., 2006). Once the daily evaluation of the dataset was performed

337 successfully, we handled the time series analysis step by treating the cam-
338 paign and continuous sites differently. For those have 24 hr observations for
339 365 day in a year, instead of applying a Global Kalman filter (the GLOBK
340 part of the above-mentioned software), we adopted a different strategy to
341 obtain a revised position time series and associated errors. We explain the
342 details of this below.

343 The signals at two thirds of the continuous GPS sites used in our study
344 consist of uniform velocities with repetitive seasonal signatures superim-
345 posed. They are well matched by linear terms, accounting for the velocities,
346 combined with sinusoids having yearly and half-yearly periods. Seasonal
347 signals are yearly but tend to be asymmetric about their maximum and min-
348 imum values, indicating that higher order harmonics contribute. Adding
349 lower amplitude sinusoids with half-yearly periods proved sufficient to ob-
350 tain good fits. For such sites there is no need to follow standard practice of
351 adding random noise to obscure seasonal effects, because the seasonal con-
352 tributions are predictable. However, without large amplitude noise that is
353 statistically independent at each time sample, conventional regression anal-
354 ysis tends to underestimate velocity standard errors. Our remedy for this
355 problem is explained below.

356 First, we tidy outlying observations by adding the squares of the misfits to
357 the predictions to the variances of all observations. This perturbs the weights
358 assigned to the observations, so we iterate until convergence is achieved. It
359 increases the regression-analysis velocity variances by a factor of ~ 2 , given
360 typical misfits to the observations of order one standard error. Our median
361 and mean root-mean-square normalized misfits for good sites are 0.99 and
362 1.10. For the other third of sites (discussed below) these numbers increase
363 to 2.03 and 2.22. Even increasing variances by factors of 5 or 10 is far
364 from enough to get round the key issue with conventional regression. Linear
365 regression analyses work from the premise that observations are statistically
366 independent. GPS observations, however, are strongly correlated one way
367 for 6 months of each year and strongly correlated the other way for the other
368 6 months.

369 How many truly independent observations are there in a continuous GPS
370 time series? Our conservative presumption for the number of truly inde-
371 pendent observations in a continuous GPS time series is that there are only
372 two per year when seasonal terms are the dominant nonlinear contribution.
373 True velocity variances are inversely proportional to the number of statisti-
374 cally independent observations. Our main step is to multiply the increased

375 regression-analysis variances from the first step by the total number of ob-
376 servations and then divide by the number of 6-monthly periods. The net
377 result for time series of order 10 years is velocity standard errors of order 0.1
378 mm/year, versus standard errors of order 0.01 mm/year without our main
379 step. In comparison, velocity standard errors from adding noise to obscure
380 seasonal effects are 5-10 times larger than our final values.

381 To validate our simple estimates of velocity standard errors, we performed
382 Monte Carlo trials with 100,000 randomly chosen subsets of the observations
383 at each site. Observations in each subset were restricted to be at least 6
384 months apart. Otherwise, all observations had the same chance of being
385 chosen, and the subsets were expanded until no more observations could be
386 added without violating the restriction. Then velocity estimates were ob-
387 tained from the subsets by simple straight-line regression. For each site that
388 gave a probability distribution of velocities. Even at bad sites the velocity
389 standard deviations agreed with our simple standard error estimates. Apart
390 from generally having worse misfits in our original regression analysis, what
391 distinguished bad sites from good sites most clearly was the shapes of their
392 velocity probability distributions. Good sites have distributions close to be-
393 ing normal in the statistical sense, whereas bad sites overall do not.

394 The third of continuous GPS sites we are referring to as bad have one or
395 more of the following issues: non-repetitive seasonal signals, short-term per-
396 turbation to the pattern of movement, and long-lasting changes in apparent
397 velocity. With less than a handful of exceptions, the conventional approach
398 of adding sufficient random noise to obscure deviations from straight-line fit
399 gives velocity standard errors large enough to cover whatever the true veloci-
400 ties might be at these sites. The few exceptions are dealt with by hand. The
401 worst case ANKR has apparent changes in velocity 10 times larger than the
402 noise added GLOBK standard error. To bring those apparent changes within
403 two standard deviations we have increased the GLOBK standard errors by
404 a factor of 5.

405 The raw position time series of survey mode sites, on the other hand, has
406 been assessed with two main steps. We adopted a first-order Gauss Markov
407 Extrapolation (Herring et al., 2018), embedded into GAMIT/GLOBK soft-
408 ware, whereby we generated the velocities and their raw sigma values for each
409 survey mode site. Once we obtained those, in the second step we followed
410 another route to obtain more realistic standard errors by appropriately scal-
411 ing them. The scaling was carried out by anchoring the campaign sites to
412 the continuous network by using a block model inversion that involves very

413 small blocks. At that point we would like to refer that this block model does
414 not aim to approach any tectonic problem but rather invert for the poles of
415 rotations for small collections of GPS sites sufficiently close to each other so
416 that they are almost guaranteed to obey the same rotation. The aim here
417 is to do a grid search (Press et al., 2007) for a scaling factor for the errors
418 of the campaign sites by keeping the errors of the continuous sites constant.
419 The result indicates a necessary increase of errors by a factor of 2.2. A quite
420 similar approach was adopted by Beavan et al. (2016) and they documented
421 a very similar error scaling factor as well.

422 *3.2. Unifying Velocity Fields*

423 This study mainly focused on the southern part of Turkey and Cyprus,
424 boundary conditions, therefore, coming from giant plates such as Nubia and
425 Arabia, are the key factors to address this problem in the kinematic context.
426 To utilize these additional constraints the region of interest was expanded
427 towards both south and east directions. To do so, we incorporated the previ-
428 ously published velocities into our model once the data processing was carried
429 out successfully. Not only in terms of areal expansion, this also enables higher
430 spatial resolution within Cyprus and Anatolia.

431 The Levant fault, which has an approximately N-S orientation from the
432 south of the Sinai Peninsula to Kahramanmaraş triple junction, is the one
433 of the most known tectonic features and there are various studies have been
434 performed to present its strain regime by taking advantage of space based
435 measurement systems. Alchalbi et al. (2010), for instance, aims to deter-
436 mine the current kinematic behavior of the northern part of the fault with
437 survey-mode GPS sites. Their velocity field lies down the western part of
438 the Arabian plate and east of the Sinai. On the other hand, Le Beon et al.
439 (2008) has concentrated on the southern part of this fault system and it ad-
440 dressed the slip behavior along the fault. Al Tarazi et al. (2011) revealed the
441 locking regime through both Wadi Arabia and Jordan Valley segments, and
442 Sadeh et al. (2012) derives the slip rates along the various segments of the
443 Levant fault by using both permanent and survey-mode GPS sites. Gomez
444 et al. (2020) is a recent study constructing a block based kinematic model
445 with their new GPS dataset and claim that the northern part of the fault
446 accumulates lower elastic strain compared to the southern part.

447 In addition, Viltres et al. (2022) has released a high resolution velocity
448 field that shows present-day kinematic of the Arabian plate. Their results
449 pointed out both stable behavior of Arabian plate and relatively small and

450 local deformation patterns within the plate. Kurt et al. (2022) also presented
 451 an updated velocity field that covers whole Anatolia.

452 We utilized some of the station velocities published by studies mentioned
 453 above. In order for minimizing the effect of the some well-known noises
 454 such as different data evaluation strategies, pre-defined reference frames from
 455 different studies etc. we rotated all these velocity fields individually with
 456 respect to our dataset.

457 The rotation is based on a least-square approach that aims to optimize
 458 the transformation matrix of common stations for each velocity field pair.
 459 Though this approach has been applied by several studies to combine ve-
 460 locities coming from different evaluations, we made some critical changes to
 461 the weight matrix of the objective function (see Özbey et al., 2021, eq. 4).
 462 We define a new parameter r_i^{-1} to re-weight the covariance matrix by $C_i r_i^{-1}$.
 463 r_i^{-1} has been constructed as the function of both distance and number of
 464 observation. According to this;

$$r_i = \begin{cases} e^{-D_i^2/n_x*n_y}, & 1 < D_i \leq 5 \\ e^{-1/n_x*n_y}, & D_i \leq 1 \end{cases} \quad (1)$$

465 where D_i is the distance between i th common site pair and n_x and n_y is
 466 the number of observations for the related stations. Our algorithm allows
 467 utilizing a maximum of 5 km distance to decide that two sites fall into the
 468 same region. It also behaves as if they are exactly the same points for pairs
 469 of stations closer than 1km. Besides, our approach takes into account the
 470 plate boundaries during its decision-making process as well. If the related
 471 station pair is in different blocks, it directly rejects it. The second parameter
 472 is the number of epochs for each site. Here it is important to note that the
 473 number of observations of permanent sites has been postulated as 365 for a
 474 year. Each velocity field has been rotated separately by taking the velocity
 475 field obtained by this study as the reference system. The statistical outcomes
 476 of these processes were tabulated in Table 7.

477 **Figure7**

478 4. Modeling

479 Our first model, aims to determine the kinematic behavior of the Nubia-
 480 Cyprus-Anatolia tectonic system in the context of an elastic block based
 481 approach (McCaffrey et al., 2007). Such a block model involves an inverse

Table 1: The first column indicates the initial reference frame of the velocity fields coming from different studies. RMS column includes the sum of the root mean square root of the horizontal components of each common station velocity pair.

Study	Reference Frame	N. of Common Stations	RMS (mm/yr)
Le Beon et al. (2008)	ITRF00	21	0.69
Alchalbi et al. (2010)	EURA_I00	11	0.39
Al Tarazi et al. (2011)	ITRF05	22	0.93
Sadeh et al. (2012)	ITRF05	24	0.77
Viltres et al. (2022)	ARAB_I14	13	0.22
Kurt et al. (2022)	EURA_I14	65	0.57
Gomez et al. (2020)	ITRF08	20	0.96

482 problem where the unknowns are, rotations for individual blocks, spatially
 483 non-varying strain rates for each individual block, and coupling ratios on
 484 the fault node points. The model can in principle be constrained by GPS
 485 velocities, geological fault slip rates and the azimuth of these rates, and focal
 486 mechanisms. We here only used GPS data. Velocity vectors used in the
 487 inversion are shown Fig. 7 in the Arabian plate reference frame (Altamimi
 488 et al., 2017).

489 The block geometry, the surface part in fact, follows the main active fault
 490 zones (Levant fault, Cyprus Arc subduction, Kyrenia range, East Anatolian
 491 fault), which are thought to be critical in shaping the regional tectonics. The
 492 distribution of seismicity is another key feature defining some block bound-
 493 aries. Our block architecture is comparable with that in previous studies
 494 (Reilinger et al., 2006; Gomez et al., 2020) but with some differences. The
 495 older studies considered Cyprus as part of Anatolia and did not feature the
 496 Kyrenia range as a block boundary. This is justifiable as it would not have
 497 been possible to constrain the motion of a Cyprus block with the very lim-
 498 ited GPS data available on the island. The Kyrenia arc continues offshore
 499 toward Iskenderun Gulf but the Cyprus block probably does not continue
 500 further east on-shore. A concentrations of mostly extensional focal mecha-
 501 nisms is observed along a NS trend crossing Iskenderun Gulf, 30 km west
 502 of the Levant fault. We assumed this trend delineates a block boundary,
 503 separating Anatolia and the Cyprus block on its western side from a zone
 504 of complex deformation along the Levant and East Anatolian faults. As in-
 505 ternal block deformation is taken into account in the model (approximated

506 as a uniform strain field in each block) this deforming zone can defined as
507 a block. The block extends eastward along the East Anatolian fault toward
508 Malatya. The northern boundary of the block is composed of the Çardak
509 Malatya faults, which are considered active (Westaway, 2003; Sançar et al.,
510 2019; Acarel et al., 2019)(Fig. 8).

511 To the south of Cyprus lies the Sinai block which is largely under water.
512 Its motion is crucial for the kinematics of the Cyprus Arc subduction but
513 can only be constrained by velocities along the Levant coast and in Sinai.
514 However, GPS velocity fields in Levant and in Southern Sinai do not fit in the
515 same rigid block reference frame. The Levant fragment of the Sinai block may
516 be affected by deformation along the Levant fault while south Sinai may be
517 affected by extension around the Aqaba gulf. This extension cannot be well
518 accounted for in our model, which simplifies the prolongation of the Levant
519 fault into the Aqaba gulf as a vertical fault, and the subduction motion along
520 the northern edge of the block should be better constrained by the northern
521 stations. We thus removed velocity data below 30°N.

522 **Figure8**

523 Along the block boundaries, we defined 5 main dislocation sources, as
524 capable of accumulating elastic deformation, on which the coupling ratio will
525 be calculated by inversion. The Levant and East Anatolian faults, which obey
526 nearly pure strike-slip motion, are modeled as vertical planar sources. The
527 boundary between Anatolia and Malatya block is also simplified as a vertical
528 fault. However, to generate the geometry of dipping faults, such as the
529 Cyprus subduction and Kyrenia fault, we followed published interpretations
530 of seismic profiles (Aksu et al., 2005, 2021; Burton-Ferguson et al., 2005; Aksu
531 et al., 2014a; Calon et al., 2005; Hall et al., 2005; Welford et al., 2015; Feld
532 et al., 2017). We employed, moreover, the seismicity of the region, compiling
533 the earthquakes greater than $M_w = 2.8$. The earthquake locations validate
534 the geometry of the main subduction seismogenic zone between Sinai and
535 Cyprus down to 40 km but do not help define the geometry at depth of
536 Kyrenia fault between Cyprus and Anatolia.

537 We performed a series of synthetic tests to determine the optimal spatial
538 resolution of the node points for the slip rate distribution dictated by the
539 spatial coverage of the GPS data along both strikes and dip directions. To
540 this end, we used a checkerboard test whereby the main thrust interface to
541 the south of Cyprus is divided into planar cells for which we monitored the
542 level of recovery of the given slip rate boundary conditions using synthetic
543 GPS velocities at the same geographic locations as our data. We tested two

Table 2: Euler Pole Parameters estimated by this study and those coming from previous studies. Uncertainty of the parameters only available for the poles calculated directly.

Pole	Lat (°)	Lon (°)	Ω (°/Myr)	Reference
SIN - AN	32.04±1.8	38.21±2.4	-0.596±0.084	this study
SIN - AN	31.99	36.01	-1.185	Reilinger et al. (2006)
NU - AN	31.80	35.16	-1.026	this study, Altamimi et al.
NU - AN	31.67	34.83	-1.205	Reilinger et al. (2006)
CY - AN	37.56±1.4	32.65±1.9	0.726±0.116	this study

Abbreviations: SIN: Sinai, AN: Anatolia,
 NU: Nubia, CY: Cyprus

544 different average cell sizes for the thrust interface. The first involved an av-
 545 erage cell size of $35km^2$ and the second is $10km^2$. These interface geometries
 546 are given in Fig. 9A-B. The tests involved no synthetic observation noises.
 547 The results suggest that the test carried out with bigger patches given in
 548 Fig. 9C give better result than one consisting of the finer patch resolution
 549 (Fig. 9D). Here, it is also important to note that we applied a secondary test
 550 to document the contribution of the new observations in Cyprus by keeping
 551 the same grid resolution and only using a single GPS observation in Cyprus
 552 (NICO, the only site that was available prior to this study) lead to a much
 553 poorer recovery in the tests.

554 **Figure9**

555 Once we determined the block geometry and the node distribution through-
 556 out the planar fault surfaces, we carried out the inversion in two steps using
 557 TDEFNODE. First, block rotation and strain rate parameters are deter-
 558 mined by leveraging a least square inversion taking into consideration the
 559 earth’s curvature (Savage et al., 2001). Table 2 summarizes the Euler pole
 560 parameters estimated in this study as well as those given by previous studies.

561 Determining robust Euler pole parameters is of utmost importance for
 562 addressing the motion of the Cyprus arc subduction. This problem is com-
 563 plicated by the fact that a large part of the Sinai plate is underwater and
 564 that the prolongation of the Sinai plate along the Levant coast (where GPS
 565 stations are located) may be deforming. Euler poles of Sinai relative to Ana-
 566 tolia and to Arabia were obtained by the block model inversion. In order to
 567 estimate the Euler pole of the Nubia plate with respect to Anatolia we com-
 568 bined our determination of the Arabia-Anatolia pole with a Nubia-Arabia
 569 pole calculated in the ITRF No Net Rotation reference frame by Altamimi

570 et al. (2017). The Nubia poles from this study and Reilinger et al. (2006)
571 are similar to each other albeit with a slight difference in the rotation rates.
572 The location of the Euler pole of Reilinger et al. (2006) for Sinai relative
573 to Anatolia and ours are also close to each other. The rotation rate of the
574 Reilinger et al. (2006) pole, however, is markedly faster resulting in a slower
575 subduction velocity in our model. The data we used to constrain the motion
576 of the Sinai block are essentially the same as in the previous studies, but we
577 excluded data from South Sinai (below 30°N) as these cannot be fit in the
578 same rigid reference frame, and this explains in large part the differences.
579 The pole we determined provides a better fit of GPS data along the Lev-
580 ant coast, but a worse fit of the GPS data in the southern part of Sinai.
581 We believe that this pole provides a better description of the motion of the
582 Mediterranean seafloor as it subducts beneath Cyprus.

583 In the second step, on the other hand, rather than a linear inversion, a
584 series of nonlinear inversions such as grid search and simulated annealing
585 (Press et al., 2007) has been run iteratively to solve the coupling ratio on
586 each node point. The green functions that coincide with the location of
587 the GPS stations on the surface are determined with a rigorous approach
588 designating the planar fault into rectangular patches (Okada, 1992). For the
589 parametrization of fault coupling, we express the coupling ratio as constant
590 between the surface and depth z_1 (an inversion parameter at each node) and
591 decaying exponentially below, as proposed presented by Wang et al. (2003).

592 Figs. 10 and 11 represent the block motions and locking distributions
593 along the boundaries defined as dislocation sources in the model. The Cyprus
594 arc accommodates 3-6 mm/yr convergent slip rates reducing progressively
595 from west to east. The inversion estimates z_1 value around 20-25 km depth,
596 however, due to the fact that there is no GPS data for the offshore part,
597 the uncertainties of the coupling coefficient are directly associated with the
598 distance between the node points and Cyprus, which is the closest location
599 including data. The motion of the Kyrenia arc, on the other hand, is mainly
600 the left lateral strike-slip from the northwesternmost tip to the east of the
601 island with rates 3-4 mm/yr. Although the slip rates along the western
602 prolongation of the Kyrenia arc also obey a left lateral strike-slip behavior,
603 the spatial distribution of our dataset may not be considered capable of
604 resolving this particular region. Along the boundary between the Anatolian
605 and Cyprus blocks on one side and the so called Malatya block on the other
606 side, the inversion also indicates a ~ 1.3 mm/yr extensional motion, which is
607 also in agreement with the predominantly extensional style of the earthquakes

608 (see Fig. 8). Meanwhile, there are relatively larger velocity residuals on the
609 left side of the boundary, roughly coinciding with Adana Basin, that may
610 represent active deformation not properly modeled with the assumed block
611 geometry. Where the block boundary changes its azimuth from N-S to E-
612 W and along the Çardak fault behaves as an almost left lateral strike slip
613 behavior with a 1.8 mm/yr rate. The Malatya fault, which extends from the
614 eastern tip of the Çardak fault towards the north, has also left lateral strike
615 slip motion accounting for 1.7 mm/yr. The motion on the East Anatolian
616 fault zone, on the other hand, decreases from 6.2 to 5 mm/yr from Elazığ
617 to Kahramanmaraş triple junction where it connects with the Levant fault.
618 Some additional shear is taken up by internal deformation of the Malatya
619 block.

620 **Figure10**

621 **Figure11**

622 4.1. Strain rates

623 In this section, we will determine a contemporary strain rate field to
624 characterize deformation styles in the region that comprises northeast Nubia,
625 eastern Mediterranean Sea, Dead Sea fault zone, Cyprus, Cilicia basin and
626 neighboring southern Turkey. Our aim is to shed light on its kinematics.
627 This can be useful for future dynamical models as kinematic constraints. In
628 the kinematic continuum model, which is based on the method described
629 by Haines and Holt (1993); Beavan and Haines (2001), we aim to find the
630 minimum strain rate field that best fits the GPS velocity field for the model
631 region by minimizing the following objective function:

$$\sum_{\text{cells}} \nu \left(\dot{\bar{\varepsilon}}_{\phi\phi}^2 + 2\dot{\bar{\varepsilon}}_{\phi\theta}^2 + \dot{\bar{\varepsilon}}_{\theta\theta}^2 \right) S \quad (2)$$

632 where $\bar{\varepsilon}_{\phi\phi}^{\text{obs}}$, $\bar{\varepsilon}_{\phi\theta}^{\text{obs}}$, and $\bar{\varepsilon}_{\theta\theta}^{\text{obs}}$ are strain rate tensor components with respect
633 to longitude θ and latitude ϕ for each cell, S corresponds to the surface area of
634 the related cell. Even though there is a possibility to prescribe the ν value,
635 which is a weighting factor associated with the rheology of the deforming
636 material, for each cell individually, we employed a single uniform ν value for
637 all the cells within the domain. In practice however the weak form of the
638 function mentioned above can be expressed as

$$\sum_{\text{elements}} \iint \nu \left(\dot{\bar{\varepsilon}}_{\phi\phi}^2 + 2\dot{\bar{\varepsilon}}_{\phi\theta}^2 + \dot{\bar{\varepsilon}}_{\theta\theta}^2 \right) dS \quad (3)$$

639 Eq.3 represents the simplified penalty function of this rigorous approach,
640 further details can be found in Beavan and Haines (2001), Appendix 5.

641 Here, we solely utilized the GPS velocity field without imposing any plate
642 motion boundary conditions Fig 12. As mentioned above, we prescribed a
643 homogeneous ν value to achieve a $\tilde{\chi}^2$ score around unity. Experiments were
644 made using larger ν values in the grid cells in SW Cyprus and further offshore
645 where seismic catalogues show the clustering of earthquakes. If these are
646 “damage” zones their bulk deformability might be higher than other zones.
647 However these experiments did not significantly improve the fit to the GPS
648 velocities even in the near field sites in southern Cyprus.

649 **Figure12**

650 The solution indicates, in general, small strain rates within Cyprus, the
651 second invariant rarely exceeding 20 nanostrains per year. However there
652 is a clear spatial variability of deformation styles on the island. To the
653 south of the Kyrenia range roughly N-S compression dominates while to the
654 north transpressive strike slip regime is found. On a larger scale, this strain
655 partitioning within Cyprus seems to act as a diffuse transition that rotates
656 the predominant compression from NW-SE in the Sinai block onto NE-SW
657 in the Cilicia basin immediately to the north of Cyprus. The solution does
658 not resolve strike slip deformation in the southwest of Cyprus where some
659 studies suggest the presence of two active shear zones, NNE trending Gazibaf
660 Transform to the west of Cyprus and Biruni fault trending NW offshore to
661 the NW of Cyprus (Seyitoğlu et al., 2022). The lack of GPS data probably
662 leads us to a strain rate field much smoother than the reality in Cilicia basin
663 but on the large scale, the solution shows a compressive to transpressive
664 regime with NE-SW to N-S compression offshore to the northwest of Cyprus.
665 The shortening integrated along the principal strain axis between the coasts
666 of Cyprus and Turkey amounts to a maximum of 0.8 mm/yr. In Türkiye, a
667 swath of higher strain rate (more than 30 nanostrain/yr) over a width of 50-60
668 km is found NW of Iskenderun Gulf along the EAF trend, thus defining a East
669 Anatolian shear zone. There, principal strain directions (E-W extension and
670 N-S compression) are consistent with left lateral strike-slip motion and they
671 retain the same orientation westward all the way to Taurus and Adana/Cilicia
672 Basin. The areal strain is positive except at a few locations, indicating
673 transtensive to extensional deformation, consistent with focal mechanisms.
674 In the Taurus itself, strain is low (less than 10 nanonstrain/year) but display
675 consistent principal axis with NE-SW compression and NW-SE extension,
676 respectively parallel and perpendicular to the mountain range trend. Zones

677 of higher strain appear to correlate with zone of higher seismic activity Fig.
678 13. In the East Anatolian shear zone, seismicity appears maximal on the
679 sides of the zones, where the block boundaries were drawn. In the Taurus,
680 seismicity is comparatively lower but one occurs in the prolongation of the
681 Tuz Gölü Fault (Özbey et al., 2022), two others are located along the coast.
682 Areal strain is dominantly positive, but changes sign in Mut Basin. This is
683 the only part of Taurus where compressive strain is observed, and this occurs
684 at a slow rate. Some transpression may also occur beneath Adana Basin.
685 From south of Turkey along the coast towards Israel, there is very poor GPS
686 coverage. The dominating principal strain orientations are consistent with
687 left-lateral shear on the Levant fault. In Israel where the GPS coverage is
688 very dense, but still mostly located on the western side of the Levant fault,
689 we see some short wavelength variability of the strain rate field with the
690 compressional axes trending largely NW-SE. The strain rates become less
691 coherent towards the southern tip of Israel.

692 **Figure13**

693 **5. Discussion**

694 This study mainly focuses on the present-day kinematics around Kahra-
695 manmaraş triple junction, in particular Cyprus, southern Turkey, and the
696 Adana/Cilicia Basin therein. To this end, we densified the current GPS net-
697 work and performed periodical observations to gather further information
698 about the current tectonic situation of the area. Furthermore, we enriched
699 our dataset with published velocities by several studies carried out recently.
700 The geologic evolution of the region has been rigorously addressed in the
701 second chapter. Here, we discuss our model outcomes by comparing them
702 with previous studies.

703 *5.1. Kinematics*

704 Block based model inversion indicates that the Levant fault accommo-
705 dates 3-4 mm/yr slip rate, and it also increases, slightly but steadily, from
706 north to south. Our results mainly coincide with older studies such as
707 Wdowinski et al. (2004); Gomez et al. (2007); Sadeh et al. (2012), but some-
708 what differs with other studies which found slightly faster motion (Alchalbi
709 et al., 2010; Gomez et al., 2020). Meanwhile, it is important to remind that
710 we have no new observations in the vicinity of the Levant Fault, aside from

711 new IGS sites, and our inversion leveraged the combination of published ve-
712 locities. In our results, slip from Gulf of Aqaba to Dead Sea accounts for 3.9
713 mm/yr with an almost purely left lateral strike slip regime. However, the
714 fault orients to the northeast, towards Palmyra mountains in fact, although
715 the slip rate has still a strike domination with a 3.4 mm/yr rate, it also
716 accommodates a 1.2 mm/yr compressional rate. Gomez et al. (2020) find
717 a decreasing motion northward from 5.0 mm/yr to 2.5-3.5 mm/yr as they
718 consider 2 additional blocks transferring part of the Levant fault motion to
719 hypothetical offshore structures Gomez et al. (2020). In fact, we do not find
720 that these additional boundaries are needed to fit the GPS data acquired be-
721 tween the Levant fault and the Mediterranean coast. However, the removal
722 of data from South Sinai in our analysis may explain some of the differences
723 between the modeling results.

724 The new observations within Cyprus shed some light to comprehend not
725 only the deformation within Cyprus but also the current behavior of the
726 subduction. The slip characteristic both on Cyprus arc and Kyrenia range
727 indicates that an ongoing shear partitioning is the dominant regime for the
728 area. The subduction is still active in spite of the incipient collision with the
729 Eratosthenes Seamount, with near frontal convergence at a 6.0 mm/yr rate
730 southwest of Cyprus. The locking depth (z_1) extends from the surface to 20
731 km depth, which is consistent with Welford et al. (2015); Feld et al. (2017).
732 We find a nearly pure left-lateral strike-slip motion on Kyrenia range with
733 a rate of 4.2 mm/yr, suggesting a nearly perfect shear partitioning between
734 the subduction and Kyrenia range. Previous block models (Reilinger et al.,
735 2006; Gomez et al., 2020) have a Sinai/Anatolia rotation pole close to ours
736 but treated Cyprus as part of the Anatolia block because of insufficient GPS
737 data on Cyprus. This pole only predicts moderate obliquity on the Cyprus
738 subduction, about 20° south of Cyprus, which corresponds to the critical
739 obliquity threshold for the onset shear partitioning above a subduction zone
740 (McCaffrey, 1992). The rotation motion of Anatolia vs Sinai and the arc
741 shape of the subduction cause a lateral variations of obliquity so that 20° is
742 a minimum value, but shear partitioning above a subduction should should
743 not in principle lower slip vector obliquity below $15-20^\circ$ (McCaffrey, 1992).
744 It is thus possible that forces applied on the E and W boundaries of Cyprus
745 block play a role. the Cyprus block interacts with the Malatya block at its
746 NE end and conditions on this boundary are extensional. It is thus possible
747 that the forces applied in this zone near the triple junction influence the
748 motion of the Cyprus block and particularly the amount of strike-slip taken

749 up in Kyrenia range.

750 The Malatya block is involved in shear partitioning in the East Anatolian
751 shear zone. Its southern boundary is the East Anatolian fault and Levant
752 fault zones. Its northern boundary corresponds to the Çardak and Malatya
753 faults. On the the East Anatolian fault (southern boundary of the Malatya
754 Block), we obtain 5-6.2 mm/yr strike-slip rates that are lower than previous
755 studies (Aktug et al., 2016; Reilinger et al., 2006). However, these studies
756 considered a single fault. The strike-slip rate on the Malatya fault we obtain
757 (1.7 mm/yr) is consistent with previous studies (Aktuğ et al., 2013). The
758 strike-slip rate on the Çardak fault we obtained from the block model is
759 1.8 mm/yr and is comparable with a 2 mm/yr slip rate calculated from
760 geomorphological offsets (Westaway, 2003). In addition, the principal strain
761 orientations between these two faults indicate left-lateral shear co-linear with
762 shear along the East Anatolian fault zone (see Figs. 11 and 12) with an
763 average rate of 35 nanostrain per year (the non-varying strain rate parameter
764 of the Malatya block). Assuming simple shear, the internal deformation of
765 the Malatya block over an average width of 50 km amounts to about 1.7
766 mm/yr. The strike-slip motion between Anatolia and Arabia thus appears
767 to be distributed between the East Anatolian fault, the faults defining the
768 northern boundary of the Malatya block and internal deformation of the
769 block. These three components add up to 8.5-9.7 mm/yr, which is consistent
770 with previous studies.

771 An earthquake sequence Feb 6 2023 ruptured both boundaries of the
772 deforming Malatya block. The main shock (M_w 7.8) occurred on the East
773 Anatolian and Levant faults while a large M_w 7.6 aftershock occurred on
774 Çardak Faults, corresponding to a moment magnitude about half of that of
775 the main shock. However preliminary estimates of coseismic slip from finite
776 fault models and from optical image correlation indicate that the smaller
777 earthquake has in fact larger displacements but over a smaller rupture length.
778 The occurrence of these events shows that both boundaries are seismically
779 active and present a high seismic hazard but also suggest that recurrence
780 interval is very different on these two faults. Early estimates of surface slip
781 from Sentinel-2 image correlation are 4 m in average over a large part of the
782 main shock rupture with a local maximum of about 7 m, and 6 m in average
783 for the aftershock with a maximum of 8-9 m. Assuming these earthquakes
784 are characteristic of the segment they ruptured and using our interseismic
785 backslip estimates, recurrence intervals of 750 to 1500 year are inferred for
786 the East Anatolian Fault and from 3000 to 5000 years on the Çardak Fault.

787 It thus appears that triggering of the Çardak Fault does not occur each
788 time a large earthquake occurs on the East Anatolian Fault, and probably
789 less than once every three cycle. It also appears likely that the M_w 7.8
790 earthquake has a longer recurrence interval than characteristic earthquakes
791 on segments further east on the East Anatolian Fault. These segments are
792 shorter, with lower magnitude characteristic earthquakes (Aktug et al., 2016)
793 and the slip rate on the East Anatolian Fault increases eastward because
794 shear partitioning decreases away from the Kahramanmaraş triple junction.

795 5.2. *Tectonics*

796 Fig. 12 shows the strain vector field and it has a nearly perfect agreement
797 with the active structures displayed in Fig. 4. In other words, two completely
798 independent data sets show precisely the same pattern of deformation. This
799 is quite astonishing in such a complexly deforming region. The basic message
800 they give is that the area between Lebanon and the Troodos mountains is
801 shortening essentially perpendicularly to the mapped active tectonic struc-
802 tures that strike generally east-west. Between Cyprus and Turkey the ver-
803 gence of the thrusts is northward. Offshore Lebanon they are north and west-
804 ward. When the strikes bend northward, shortening gives way to extension
805 because of the activity of the Kahramanmaraş and the Hatay triple junctions,
806 as predicted by the model of Şengör et al. (1980); Şengör et al. (1985, 2019).
807 When we cross the Mesaoria plain, the strain vectors and the structures indi-
808 cate roughly north-south shortening and east-west stretching. However,
809 here the strain arrows refine the picture presented by the tectonic structures
810 by showing that in the Kyrenia Range the shortening is north-northeast and
811 the stretching is perpendicular to it; moreover the shortening strain increases
812 from east to west. Within the Adana-Cilicia basin the same pattern is main-
813 tained. In the western part of the basin the normal faults faithfully reflect the
814 stretching direction. Farther east the situation becomes more complicated
815 and the normal faults have increasing components of obliquity along them.
816 This is hardly surprising, as east of Mersin the faults closely follow the south-
817 ern continental margin of Turkey as it abuts against the common delta of
818 Seyhan and Ceyhan. The strain styles indicate some transpression in Adana
819 Basin but there is little evidence supporting active thrusting along the Tau-
820 rus range. But now, then north-south faults between the Hatay Rift and the
821 Misis-Andirin trend show normal faulting along west-dipping listric faults as
822 deduced from the locations of the earthquake epicentres and the fault out-
823 crops: when the fault dips are plotted against earthquake hypocentres they

824 pass beneath them when continued westward. So, they must listrically bend
825 to meet the earthquake hypocentres (Jackson and McKenzie, 1983). When
826 we step outside the Adana/Cilicia basin to the north, onto the karst plateaux
827 of the central Taurus, the structures become much scarcer and there we are
828 entirely dependent on the strain vectors supplied by the GPS to obtain a
829 picture of the total deformation. As we argued above, this is not to say that
830 no deformation is taking place north of the Adana/Cilicia Basin. The earth-
831 quake hypocentres in our Fig. 6 also support that the deformation that once
832 used to be more widespread in the Taurus had migrated out southward into
833 the Adana/Cilicia basin and Cyprus thus diminishing the deformation inten-
834 sity under the karst plateaux. The gravity potential of Taurus plateau causes
835 compressive stresses within the Adana/Cilicia basin in front of it while the
836 basin is stretched east-west because of the westward escape of Central and
837 Western Anatolia with respect both to Eurasia and Afro-Arabia. Thus the
838 Adana/Cilicia basin is not a forearc basin, has never been one since the late
839 Cretaceous obduction in Cyprus (Şengör, 2014, see), but a flexural molasse
840 basin related to the closure of the Inner Tauride Ocean (Şengör et al., 2019)
841 that is being stretched east-west as a consequence of the escape of Anatolia.
842 The stretching even created some mafic magmatism in the eastern part of
843 the basin (Polat et al., 1997; Parlak et al., 1998). The only similar situation
844 that we know of is that of the Eastern Venezuelan basin within the Humboldt
845 keirogen, which is being shortened north-south and stretched east-west owing
846 to the eastward escape of the Caribbean plate with respect to South America
847 (Burke et al., 1978; Şengör et al., 2019). The Hegau volcanoes in the Molasse
848 of the Central Alps are also in a similar setting, in the far western part of
849 the Molasse Basin, but there we do not have the corresponding strike-slip
850 tectonics (see Hofmann, 1968, especially fig 1).

851 The continuum deformation field obtained in and around the Taurus
852 mountain range shows little shortening in the upper crust and does not
853 support active thrusting along its topographic front toward Adana Basin.
854 Cyprus/Anatolia motion in the block model is mostly strike-slip. This mo-
855 tion is in large part taken up on the Kyrenia range but residuals of the block
856 model suggest left lateral strike-slip motion is also taking place along the
857 coast of Cilicia Basin. In fact the Anatolia-Cyprus pole would predict pure
858 strike-slip relative motion on a fault running along this coast, which nearly
859 follows a small circle for the pole we determined. There is thus little con-
860 vergence left from the motion of Cyprus to explain the high uplift rates of
861 Taurus since mid-Pleistocene. It is possible that these high uplift rates are

862 enhanced by erosion as they are measured near rivers that incise the southern
863 slope of the Taurus range at a very high rate. Notably the rapid incision of
864 the Göksu river in the Mut Basin may feed back on the uplift of the adjacent
865 plateaux, where the highest uplift rates were reported (see Öğretmen et al.,
866 2018). The convergence of Nubia and Anatolia may still play a significant
867 role. We pointed out that the lithosphere being subducted beneath Cyprus is
868 continental and hence that thinned continental crust is subducting beneath
869 Cyprus and possibly as far as beneath Central Taurus. The underthrusting
870 of continental lithosphere beneath Taurus may thus contribute to its contin-
871 ued uplift even in the apparent absence of convergence. Drawing again on
872 the comparison with the Alps, this situation may be analogous with the un-
873 derplating and exhumation of the Briançonnais in the Oligocene (e.g. Jolivet
874 et al., 2003). It has been proposed that slab break off occurred concurrently
875 in the Alps, and also caused magmatism but this hypothesis may be consid-
876 ered untestable (Garzanti et al., 2018). In the Taurus as in the Alps, there
877 are other processes by which lower crust and mantle could influence the uplift
878 rates.

879 **6. Conclusion**

880 Acquisition of new GPS data on Cyprus and Southern Turkey bring new
881 insight on the deformation of the Kahramanmaraş triple junction, Cyprus
882 Arc, and Taurus. Although the modeling performed in this study is limited
883 by the large areas underwater around Cyprus, it shows that the present day
884 deformation of the island may be understood as a shear partitioning system
885 between the Cyprus arc subduction and the Kyrenia range, which appears
886 to be a dominantly strike-slip boundary. The incipient collision with the
887 Eratosthenes seamount may not have yet perturbed much the kinematics
888 of the Cyprus subduction. However, the northeastward prolongation of the
889 Cyprus block toward the Anatolia/Arabia collision zone, is a zone of complex
890 deformation north and east of the Levant fault and East Anatolian Fault.
891 The main conclusion of this study is thus the extreme complexity caused
892 by the collision of two continents one of which is flanked by an ocean. The
893 presence of oceanic lithosphere makes escape possible which creates a strike-
894 slip regime, where, in a case of flush collision, would not exist where it does
895 here. Pre-existing structures somewhat complicate this neat picture and it
896 is therefore important to be aware of them. When one imagines the further
897 complexity that will ensue when the collision is complete, i.e., all oceanic

898 lithosphere is consumed, one can appreciate how naïve most of our orogenic
899 evolution models must be. No prêt-à-porter model can be appropriate for
900 any tectonic environment and interpretations must be based on all available
901 local geological data, interpreted in the light of general models, which most
902 likely would necessitate more or less extensive modifications. In our case
903 the complete failure of the fore-arc model is a fine illustration of this princi-
904 ple. Neither any numerical model can hope to be successful if it ignores the
905 geology on the ground.

906 **Acknowledgements**

907 This study was funded by Istanbul Technical University Scientific Re-
908 search Projects Coordination Unit as MGA-2020-42584 ID Number research
909 project. Moreover, it is part of the Ph.D. thesis of the corresponding author.
910 The modeling part was carried out mostly at Centre Européen de Recherche
911 et d'Enseignement des Géosciences de l'Environnement (CEREGE) in the
912 scope of the TUBITAK 2214A International Research Scholarship during
913 Ph.D. for Ph.D. candidates program with the project number 1059B142000638.
914 The calculation of daily coordinates of GPS sites reported in this paper were
915 performed at TUBITAK ULAKBIM, High Performance and Grid Computing
916 Center (TRUBA resources).

917 We would like to thank the T.C. Ministry of Defence General Directorate
918 of Mapping for their contribution during the field studies and shared previous
919 GPS observations measured by them. We are grateful to Ali Fahri Ozten and
920 Sebat Proje ve Muhendislik for the instrument supplying and accommodation
921 in Cyprus. We also want to thank Fatih Taskiran, Mert Topal and Dr. Ali
922 Ihsan Kurt for their priceless effort during the field observations.

923 Dr. Robert McCaffrey's remarks guided us especially establishing the
924 block model. We also thank Xavier Le Pichon and Solène Antoine for their
925 comments and discussions on the understanding of the recent earthquakes.
926 We are also grateful to Dr. Timothy Kusky for his support.

927 **References**

928 Acarel, D., Cambaz, M.D., Turhan, F., Mutlu, A.K., Polat, R., 2019.
929 Seismotectonics of malatya fault, eastern turkey. *Open Geosciences* 11,
930 1098–1111. URL: <https://doi.org/10.1515/geo-2019-0085>, doi:doi:
931 10.1515/geo-2019-0085.

- 932 Aksu, A., Calon, T., Hall, J., Kurtboğın, B., Gürçay, S., Çifçi, G., 2014a.
933 Complex interactions fault fans developed in a strike-slip system: Kozan
934 fault zone, eastern mediterranean sea. *Marine Geology* 351, 91–107.
- 935 Aksu, A., Calon, T., Hall, J., Mansfield, S., Yaşar, D., 2005. The cilicia–
936 adana basin complex, eastern mediterranean: Neogene evolution of an
937 active fore-arc basin in an obliquely convergent margin. *Marine Geology*
938 221, 121–159.
- 939 Aksu, A., Hall, J., Yaltırak, C., 2021. Miocene–quaternary tectonic, kine-
940 matic and sedimentary evolution of the eastern mediterranean sea: A re-
941 gional synthesis. *Earth-Science Reviews* 220, 103719.
- 942 Aksu, A., Walsh-Kennedy, S., Hall, J., Hiscott, R., Yaltırak, C., Akhun,
943 S., Çifçi, G., 2014b. The pliocene–quaternary tectonic evolution of the
944 cilicia and adana basins, eastern mediterranean: Special reference to the
945 development of the kozan fault zone. *Tectonophysics* 622, 22–43.
- 946 Aktug, B., Ozener, H., Dogru, A., Sabuncu, A., Turgut, B., Halicioglu, K.,
947 Yilmaz, O., Havazli, E., 2016. Slip rates and seismic potential on the
948 east anatolian fault system using an improved gps velocity field. *Jour-
949 nal of Geodynamics* 94-95, 1–12. URL: <https://www.sciencedirect.com/science/article/pii/S0264370716300102>, doi:<https://doi.org/10.1016/j.jog.2016.01.001>.
- 952 Aktuğ, B., Parmaksız, E., Kurt, M., Lenk, O., Kılıçoğlu, A., Gürdal, M.A.,
953 Özdemir, S., 2013. Deformation of central anatolia: Gps implications.
954 *Journal of Geodynamics* 67, 78–96. URL: <https://www.sciencedirect.com/science/article/pii/S0264370712000920>, doi:<https://doi.org/10.1016/j.jog.2012.05.008>. wEGENER 2010.
- 957 Al Tarazi, E., Abu Rajab, J., Gomez, F., Cochran, W., Jaafar, R., Ferry,
958 M., 2011. GPS measurements of near-field deformation along the south-
959 ern Dead Sea Fault System. *Geochemistry, Geophysics, Geosystems* 12.
960 URL: <https://doi.org/10.1029/2011GC003736>, doi:<https://doi.org/10.1029/2011GC003736>.
- 962 Alan, I., Bakirhan, B., Elibol, H., 2012. 1:100000 scale geological maps of
963 turkey no:165, karaman n-32 quadrangle.

- 964 Alan, I., Balci, V., Sahin, S., Boke, N., Esirtgen, T., 2013. 1:100000 scale
965 geological maps of turkey no:194, silifke o-32 quadrangle.
- 966 Alan, I., Sahin, S., Bakirhan, B., 2011. 1:100000 scale geological maps of
967 turkey no:166, adana n-33 quadrangle.
- 968 Alchalbi, A., Daoud, M., Gomez, F., McClusky, S., Reilinger, R., Romeyeh,
969 M.A., Alsouod, A., Yassminh, R., Ballani, B., Darawcheh, R., Sbeinati, R.,
970 Radwan, Y., Masri, R.A., Bayerly, M., Ghazzi, R.A., Barazangi, M., 2010.
971 Crustal deformation in northwestern Arabia from GPS measurements in
972 Syria: Slow slip rate along the northern Dead Sea Fault. *Geophysical*
973 *Journal International* 180, 125–135. URL: [https://doi.org/10.1111/j.](https://doi.org/10.1111/j.1365-246X.2009.04431.x)
974 [1365-246X.2009.04431.x](https://doi.org/10.1111/j.1365-246X.2009.04431.x), doi:10.1111/j.1365-246X.2009.04431.x.
- 975 Altamimi, Z., Métivier, L., Rebischung, P., Rouby, H., Collilieux, X., 2017.
976 ITRF2014 plate motion model. *Geophysical Journal International* 209,
977 1906–1912. doi:10.1093/gji/ggx136.
- 978 Ayhan, A., 1988. 1:100000 olcekli acinsama nitelikli turkiye jeoloji haritalari
979 serisi, kozan-j21 paftasi.
- 980 Bassant, P., Van Buchem, F., Strasser, A., Görür, N., 2005. The stratigraphic
981 architecture and evolution of the burdigalian carbonate—siliciclastic sed-
982 imentary systems of the mut basin, turkey. *Sedimentary Geology* 173,
983 187–232.
- 984 Beavan, J., Haines, J., 2001. Contemporary horizontal velocity and strain
985 rate fields of the Pacific-Australian plate boundary zone through New
986 Zealand. *Journal of Geophysical Research: Solid Earth* 106, 741–770.
987 doi:10.1029/2000jb900302.
- 988 Beavan, J., Wallace, L.M., Palmer, N., Denys, P., Ellis, S., Fournier, N.,
989 Hreinsdottir, S., Pearson, C., Denham, M., 2016. New Zealand GPS ve-
990 locity field: 1995–2013. *New Zealand Journal of Geology and Geophysics*
991 59, 5–14. doi:10.1080/00288306.2015.1112817.
- 992 Bilgic, T., 2009. 1:100000 scale geological maps of turkey no:129, karaman
993 n-31 quadrangle.
- 994 Bilgin, A.Z., 2013. 1:100000 scale geological maps of turkey no:195, mersin
995 o-35 quadrangle.

- 996 Biryol, B.C., Beck, S.L., Zandt, G., Ozacar, A.A., 2011. Segmented African
997 lithosphere beneath the Anatolian region inferred from teleseismic P-wave
998 tomography. *Geophysical Journal International* 184, 1037–1057. doi:10.
999 1111/j.1365-246X.2010.04910.x.
- 1000 Boehm, J., Werl, B., Schuh, H., 2006. Troposphere mapping functions
1001 for GPS and very long baseline interferometry from European Centre
1002 for Medium-Range Weather Forecasts operational analysis data. *Journal of Geophysical Research: Solid Earth* 111. URL: <https://doi.org/10.1029/2005JB003629>, doi:<https://doi.org/10.1029/2005JB003629>.
- 1005 Burke, K., Fox, P.J., Şengör, A.M.C., 1978. Buoyant ocean floor and
1006 the evolution of the caribbean. *Journal of Geophysical Research: Solid Earth* 83, 3949–3954. URL: <https://agupubs.onlinelibrary.wiley.com/doi/abs/10.1029/JB083iB08p03949>, doi:<https://doi.org/10.1029/JB083iB08p03949>.
- 1010 Burton-Ferguson, R., Aksu, A., Calon, T., Hall, J., 2005. Seismic stratigraphy and structural evolution of the adana basin, eastern mediterranean. *Marine Geology* 221, 189–222.
- 1013 Calon, T., Aksu, A., Hall, J., 2005. The neogene evolution of the outer latakia basin and its extension into the eastern mesaoria basin (cyprus), eastern mediterranean. *Marine Geology* 221, 61–94.
- 1016 Cipollari, P., Halasova, E., Guerbuez, K., Cosentino, D., 2013. Middle-upper miocene paleogeography of southern turkey: insights from stratigraphy and calcareous nannofossil biochronology of the olukpinar and başyayla sections (mut-ermenek basin). *Turkish Journal of Earth Sciences* 22, 820–838.
- 1021 Cosentino, D., Radeff, G., Darbaş, G., Dudas, F., Gürbüz, K., Schildgen, T., 2010. Late miocene geohistory of the mut and adana basins (southern turkey): Insight for the uplift of the southern margin of the central anatolia plateau. Middle East Technical University, Ankara, Turkey , 4–8.
- 1025 Cosentino, D., Schildgen, T.F., Cipollari, P., Faranda, C., Gliozzi, E., Hudáčková, N., Lucifora, S., Strecker, M.R., 2012. Late miocene surface uplift of the southern margin of the central anatolian plateau, central taurides, turkey. *Bulletin* 124, 133–145.

- 1029 Geological Survey Department of Cyprus, C., 2009. Digital geology of
1030 cyprus. URL: [http://www.moa.gov.cy/moa/gsd/gsd.nsf/dmlindex_](http://www.moa.gov.cy/moa/gsd/gsd.nsf/dmlindex_gr/dmlindex_gr?OpenDocument)
1031 [gr/dmlindex_gr?OpenDocument](http://www.moa.gov.cy/moa/gsd/gsd.nsf/dmlindex_gr/dmlindex_gr?OpenDocument).
- 1032 Dalkilic, H., Balci, V., 2009. 1:500000 scale geological maps of turkey, no:
1033 15 adana sheet.
- 1034 Demirtasli, E., 1984. Stratigraphy and tectonics of the area between silifke
1035 and anamur, central taurus mountains, in: Geology of the Taurus belt.
1036 International symposium, pp. 101–118.
- 1037 Demirtasli, E., TURHAN, N., Bilgin, A., Selim, M., 1984. Geology of the
1038 bolkar mountains, in: geology of the Taurus belt. International symposium,
1039 pp. 125–141.
- 1040 Dewey, J.F., 1977. Suture zone complexities: a review. *Tectonophysics* 40,
1041 53–67.
- 1042 Dewey, J.F., 2002. Transtension in arcs and orogens. *International Geology*
1043 *Review* 44, 402–439.
- 1044 Ekström, G., Nettles, M., 1997. Calibration of the hglp seis-
1045 mograph network and centroid-moment tensor analysis of signifi-
1046 cant earthquakes of 1976. *Physics of the Earth and Planetary*
1047 *Interiors* 101, 219–243. URL: [https://www.sciencedirect.com/](https://www.sciencedirect.com/science/article/pii/S0031920197000022)
1048 [science/article/pii/S0031920197000022](https://www.sciencedirect.com/science/article/pii/S0031920197000022), doi:[https://doi.org/10.](https://doi.org/10.1016/S0031-9201(97)00002-2)
1049 [1016/S0031-9201\(97\)00002-2](https://doi.org/10.1016/S0031-9201(97)00002-2).
- 1050 England, P., Houseman, G., Nocquet, J.M., 2016. Constraints from GPS
1051 measurements on the dynamics of deformation in Anatolia and the
1052 Aegean. *Journal of Geophysical Research: Solid Earth* 121, 8888–8916.
1053 URL: <https://doi.org/10.1002/2016JB013382>, doi:[https://doi.org/](https://doi.org/10.1002/2016JB013382)
1054 [10.1002/2016JB013382](https://doi.org/10.1002/2016JB013382).
- 1055 Eriş, K.K., Bassant, P., Ülgen, U.B., 2005. Tectono-stratigraphic evolution of
1056 an early miocene incised valley-fill (derinçay formation) in the mut basin,
1057 southern turkey. *Sedimentary Geology* 173, 151–185.
- 1058 Feld, C., Mechie, J., Hübscher, C., Hall, J., Nicolaidis, S., Gurbuz, C., Bauer,
1059 K., Louden, K., Weber, M., 2017. Crustal structure of the eratosthenes

- 1060 seamount, cyprus and s. turkey from an amphibian wide-angle seismic pro-
1061 file. *Tectonophysics* 700-701, 32–59. URL: <https://www.sciencedirect.com/science/article/pii/S0040195117300495>, doi:<https://doi.org/10.1016/j.tecto.2017.02.003>.
- 1064 Fernández-Blanco, D., 2014. Evolution of Orogenic Plateaus at Subduction
1065 Zones-Sinking and raising the southern margin of the Central Anatolian
1066 Plateau. Ph.D. thesis. Vrije Universiteit Amsterdam.
- 1067 Fernández-Blanco, D., Bertotti, G., Aksu, A., Hall, J., 2019. Monoclinial
1068 flexure of an orogenic plateau margin during subduction, south turkey.
1069 *Basin Research* 31, 709–727.
- 1070 Fernández-Blanco, D., Mannu, U., Bertotti, G., Willett, S.D., 2020. Forearc
1071 high uplift by lower crustal flow during growth of the cyprus-anatolian
1072 margin. *Earth and Planetary Science Letters* 544, 116314.
- 1073 Garzanti, E., Radeff, G., Malusa, M.G., 2018. Slab breakoff: A critical
1074 appraisal of a geological theory as applied in space and time. *Earth-
1075 Science Reviews* 177, 303–319. URL: <https://www.sciencedirect.com/science/article/pii/S0012825217303641>, doi:<https://doi.org/10.1016/j.earscirev.2017.11.012>.
- 1078 Gedik, A., Birgili, S., Yilmaz, H., Yoldas, R., 1979. Ge-
1079 ology of the mut- ermenek- simfke (konya, mersin) area and
1080 petroleum possibilities. *Bulletin of the Geological Society of
1081 Turkey* 22, 1–20. URL: [http://eski.jmo.org.tr/resimler/ekler/
1082 5fc52ed8f88c813_ek.pdf?dergi=TURKIYEJEOLLOJIBULTENI](http://eski.jmo.org.tr/resimler/ekler/5fc52ed8f88c813_ek.pdf?dergi=TURKIYEJEOLLOJIBULTENI).
- 1083 Gomez, F., Cochran, W.J., Yassminh, R., Jaafar, R., Reilinger, R., Floyd,
1084 M., King, R.W., Barazangi, M., 2020. Fragmentation of the Sinai Plate
1085 indicated by spatial variation in present-day slip rate along the Dead Sea
1086 Fault System. *Geophysical Journal International* 221, 1913–1940. URL:
1087 <https://doi.org/10.1093/gji/ggaa095>, doi:10.1093/gji/ggaa095.
- 1088 Gomez, F., Karam, G., Khawlie, M., McClusky, S., Vernant, P., Reilinger, R.,
1089 Jaafar, R., Tabet, C., Khair, K., Barazangi, M., 2007. Global Positioning
1090 System measurements of strain accumulation and slip transfer through the
1091 restraining bend along the Dead Sea fault system in Lebanon. *Geophysical*

- 1092 Journal International 168, 1021–1028. URL: [https://doi.org/10.1111/](https://doi.org/10.1111/j.1365-246X.2006.03328.x)
1093 [j.1365-246X.2006.03328.x](https://doi.org/10.1111/j.1365-246X.2006.03328.x), doi:10.1111/j.1365-246X.2006.03328.x.
- 1094 Gorur, N., 1994. Tectonic control in the development of a lower-middle
1095 miocene reef at a complex triple junction; depositional history of the
1096 karaisali formation of the adana basin, turkey. *Geologie Mediterranee*
1097 21, 49–67.
- 1098 Gorur, N., 2014. Sedimentology of the Karaisali limestone and associated
1099 clastics (Miocene) of the northwest flank of the Adana Basin, Turkey.
1100 Ph.D. thesis. Univ. London, Imperial Coll.
- 1101 Göğüş, O.H., Pysklywec, R.N., Şengör, A.M.C., Gün, E., 2017. Drip
1102 tectonics and the enigmatic uplift of the Central Anatolian Plateau.
1103 *Nature Communications* 8, 1538. URL: [https://doi.org/10.1038/](https://doi.org/10.1038/s41467-017-01611-3)
1104 [s41467-017-01611-3](https://doi.org/10.1038/s41467-017-01611-3), doi:10.1038/s41467-017-01611-3.
- 1105 Guvercin, S.E., Konca, A.O., Ozbakir, A.D., Ergintav, S., Karabu-
1106 lut, H., 2021. New focal mechanisms reveal fragmentation and active
1107 subduction of the antalya slab in the eastern mediterranean.
1108 *Tectonophysics* 805, 228792. URL: [https://www.sciencedirect.com/](https://www.sciencedirect.com/science/article/pii/S0040195121000767)
1109 [science/article/pii/S0040195121000767](https://www.sciencedirect.com/science/article/pii/S0040195121000767), doi:[https://doi.org/10.](https://doi.org/10.1016/j.tecto.2021.228792)
1110 [1016/j.tecto.2021.228792](https://doi.org/10.1016/j.tecto.2021.228792).
- 1111 Haines, A.J., Holt, W.E., 1993. A procedure for obtaining the com-
1112 plete horizontal motions within zones of distributed deformation from
1113 the inversion of strain rate data. *Journal of Geophysical Research* 98.
1114 doi:10.1029/93jb00892.
- 1115 Hall, J., Calon, T., Aksu, A., Meade, S., 2005. Structural evolution of
1116 the latakia ridge and cyprus basin at the front of the cyprus arc, east-
1117 ern mediterranean sea. *Marine Geology* 221, 261–297.
- 1118 Herring, T., King, R., Floyd, M., McClusky, S., 2018. Introduction to
1119 *gamit/globk*, release 10.7, *gamit/globk* documentation.
- 1120 Hofmann, F., 1968. Das moderne geologische Bild des Hegau-Vulkanismus.
1121 Max Bachmann Buchbinderei. URL: [https://books.google.fr/books?](https://books.google.fr/books?id=6KTKzgEACAAJ)
1122 [id=6KTKzgEACAAJ](https://books.google.fr/books?id=6KTKzgEACAAJ).

- 1123 Ilgar, A., Nemec, W., 2005. Early miocene lacustrine deposits and sequence
1124 stratigraphy of the ermenek basin, central taurides, turkey. *Sedimentary*
1125 *Geology* 173, 233–275.
- 1126 Jackson, J., McKenzie, D., 1983. The geometrical evolution
1127 of normal fault systems. *Journal of Structural Geology* 5,
1128 471–482. URL: [https://www.sciencedirect.com/science/article/
1129 pii/0191814183900536](https://www.sciencedirect.com/science/article/pii/0191814183900536), doi:[https://doi.org/10.1016/0191-8141\(83\)
1130 90053-6](https://doi.org/10.1016/0191-8141(83)90053-6).
- 1131 Jolivet, L., Faccenna, C., Goffé, B., Burov, E., Agard, P., 2003. Sub-
1132 duction tectonics and exhumation of high-pressure metamorphic rocks in
1133 the mediterranean orogens. *American Journal of Science* 303, 353–409.
1134 URL: <https://www.ajsonline.org/content/303/5/353>, doi:10.2475/
1135 ajs.303.5.353.
- 1136 Karabulut, H., Paul, A., Özbakır, A.D., Ergün, T., Şentürk, S., 2019. A new
1137 crustal model of the anatolia–aegean domain: evidence for the dominant
1138 role of isostasy in the support of the anatolian plateau. *Geophysical Journal*
1139 *International* 218, 57–73.
- 1140 Kelling, G., Robertson, A., Van Buchem, F., 2005. Cenozoic sedimentary
1141 basins of southern turkey: an introduction. *Sedimentary Geology* 173,
1142 1–13.
- 1143 Ketin, İ., 1983. Türkiye jeolojisine genel bir bakış. İstanbul Teknik
1144 Üniversitesi.
- 1145 Kounoudis, R., Bastow, I.D., Ogden, C.S., Goes, S., Jenkins, J., Grant, B.,
1146 Braham, C., 2020. Seismic tomographic imaging of the eastern mediter-
1147 ranean mantle: Implications for terminal-stage subduction, the uplift of
1148 anatolia, and the development of the north anatolian fault. *Geochemistry,*
1149 *Geophysics, Geosystems* 21, e2020GC009009. doi:[https://doi.org/10.
1150 1029/2020GC009009](https://doi.org/10.1029/2020GC009009).
- 1151 Kurt, I.A., Özbakır, D.A., Cingoz, A., Ergintav, S., Dogan, U., Özarpacı, S.,
1152 2022. Contemporary velocity field for turkey inferred from combination of
1153 a dense network of long term gns observations. *Turkish Journal of Earth*
1154 *Sciences* URL: <http://journals.tubitak.gov.tr/earth/>, doi:[https://
1155 doi.org/10.55730/yer-2203-13](https://doi.org/10.55730/yer-2203-13).

- 1156 Le Beon, M., Klinger, Y., Amrat, A.Q., Agnon, A., Dorbath, L., Baer, G.,
1157 Ruegg, J.C., Charade, O., Mayyas, O., 2008. Slip rate and locking depth
1158 from GPS profiles across the southern Dead Sea Transform. *Journal of Geo-*
1159 *physical Research: Solid Earth* 113. URL: [https://doi.org/10.1029/](https://doi.org/10.1029/2007JB005280)
1160 [2007JB005280](https://doi.org/10.1029/2007JB005280), doi:<https://doi.org/10.1029/2007JB005280>.
- 1161 Le Pichon, X., Şengör, A.C., İmren, C., 2019. A new approach to the opening
1162 of the eastern mediterranean sea and the origin of the hellenic subduction
1163 zone. part 2: The hellenic subduction zone. *Canadian Journal of Earth*
1164 *Sciences* 56, 1144–1162.
- 1165 Lippitsch, R., Kissling, E., Ansorge, J., 2003. Upper mantle struc-
1166 ture beneath the alpine orogen from high-resolution teleseismic to-
1167 mography. *Journal of Geophysical Research: Solid Earth* 108.
1168 URL: [https://agupubs.onlinelibrary.wiley.com/doi/abs/10.1029/](https://agupubs.onlinelibrary.wiley.com/doi/abs/10.1029/2002JB002016)
1169 [2002JB002016](https://agupubs.onlinelibrary.wiley.com/doi/abs/10.1029/2002JB002016), doi:<https://doi.org/10.1029/2002JB002016>.
- 1170 Mahmoud, S., Reilinger, R., McClusky, S., Vernant, P., Tealeb, A., 2005.
1171 Gps evidence for northward motion of the sinai block: implications for e.
1172 mediterranean tectonics. *Earth and Planetary Science Letters* 238, 217–
1173 224.
- 1174 Makris, J., Morelli, C., Zanolla, C., 1998. The bouguer gravity map of the
1175 mediterranean sea (ibcm-g). *Bollettino Di Geofisica Teorica Ed Applicata*
1176 39, 79–98.
- 1177 McCaffrey, R., 1992. Oblique plate convergence, slip vectors, and forearc
1178 deformation. *Journal of Geophysical Research: Solid Earth* 97, 8905–8915.
1179 URL: [https://agupubs.onlinelibrary.wiley.com/doi/abs/10.1029/](https://agupubs.onlinelibrary.wiley.com/doi/abs/10.1029/92JB00483)
1180 [92JB00483](https://agupubs.onlinelibrary.wiley.com/doi/abs/10.1029/92JB00483), doi:<https://doi.org/10.1029/92JB00483>.
- 1181 McCaffrey, R., Qamar, A.I., King, R.W., Wells, R., Khazaradze, G.,
1182 Williams, C.A., Stevens, C.W., Vollick, J.J., Zwick, P.C., 2007. Fault
1183 locking, block rotation and crustal deformation in the Pacific North-
1184 west. *Geophysical Journal International* 169, 1315–1340. doi:10.1111/
1185 [j.1365-246X.2007.03371.x](https://doi.org/10.1111/j.1365-246X.2007.03371.x).
- 1186 McKenzie, D., 1972. Active tectonics of the mediterranean region. *Geophys-*
1187 *ical Journal International* 30, 109–185.

- 1188 Miall, A.D., 2010. The geology of stratigraphic sequences. Springer Science
1189 & Business Media.
- 1190 Molnar, P., Tapponnier, P., 1975. Cenozoic tectonics of asia: Effects of a
1191 continental collision: Features of recent continental tectonics in asia can
1192 be interpreted as results of the india-eurasia collision. *science* 189, 419–426.
- 1193 Naylor, M., Sinclair, H., 2007. Punctuated thrust deformation in the context
1194 of doubly vergent thrust wedges: Implications for the localization of uplift
1195 and exhumation. *Geology* 35, 559–562.
- 1196 Öğretmen, N., Cipollari, P., Frezza, V., Faranda, C., Karanika, K., Gliozzi,
1197 E., Radeff, G., Cosentino, D., 2018. Evidence for 1.5 km of uplift of
1198 the central anatolian plateau’s southern margin in the last 450 kyr and
1199 implications for its multiphased uplift history. *Tectonics* 37, 359–390.
- 1200 Okada, Y., 1992. Internal deformation due to shear and tensile faults in
1201 a half-space. *Bulletin of the Seismological Society of America* 82, 1018–
1202 1040. URL: <https://doi.org/10.1785/BSSA0820021018>, doi:10.1785/
1203 BSSA0820021018.
- 1204 Özbey, V., Özeren, M.S., Henry, P., Klein, E., Galgana, G., Karabulut, H.,
1205 Lange, D., McCaffrey, R., 2021. Kinematics of the Marmara Region: a
1206 fusion of continuum and block models. *Mediterranean Geoscience Re-*
1207 *views* 3, 57–78. URL: <https://doi.org/10.1007/s42990-021-00051-y>,
1208 doi:10.1007/s42990-021-00051-y.
- 1209 Özeren, M.S., Holt, W.E., 2010. The dynamics of the eastern Mediter-
1210 ranean and eastern Turkey. *Geophysical Journal International* 183, 1165–
1211 1184. URL: <https://doi.org/10.1111/j.1365-246X.2010.04819.x>,
1212 doi:10.1111/j.1365-246X.2010.04819.x.
- 1213 Özgül, N., 1976. Some geological aspects of the taurus orogenic belt (turkey).
1214 *Bulletin of the Geological Society of Turkey* 19, 65–78.
- 1215 Parlak, O., Kop, A., Unlugenc, U.C., Demirkol, C., 1998. Geochronology and
1216 Geochemistry of Basaltic Rocks in The Karasu Graben Around Kırıkhan
1217 (Hatay), S . Turkey Geochronology and Geochemistry of Basaltic Rocks
1218 in The Karasu Graben Around Kırıkhan (Hatay), S . Turkey. *Journal of*
1219 *Geophysical Research: Solid Earth* 7, 53–62.

- 1220 Polat, A., Kerrich, R., Casey, J., 1997. Geochemistry of quaternary basalts
1221 erupted along the east anatolian and dead sea fault zones of southern
1222 turkey: implications for mantle sources. *Lithos* 40, 55–68. URL: [https://](https://www.sciencedirect.com/science/article/pii/S0024493796000278)
1223 www.sciencedirect.com/science/article/pii/S0024493796000278,
1224 doi:[https://doi.org/10.1016/S0024-4937\(96\)00027-8](https://doi.org/10.1016/S0024-4937(96)00027-8).
- 1225 Portner, D.E., Hayes, G.P., 2018. Incorporating teleseismic tomography
1226 data into models of upper mantle slab geometry. *Geophysical Journal In-*
1227 *ternational* 215, 325–332. URL: <https://doi.org/10.1093/gji/ggy279>,
1228 doi:10.1093/gji/ggy279.
- 1229 Press, W.H., Teukolsky, S.A., Vetterling, W.T., Flannery, B.P., 2007. Nu-
1230 merical recipes 3rd edition: The art of scientific computing. Cambridge
1231 university press.
- 1232 Racano, S., Jara-Muñoz, J., Cosentino, D., Melnick, D., 2020. Variable
1233 quaternary uplift along the southern margin of the central anatolian
1234 plateau inferred from modeling marine terrace sequences. *Tectonics* 39,
1235 e2019TC005921.
- 1236 Radeff, G., Schildgen, T.F., Cosentino, D., Strecker, M.R., Cipollari, P.,
1237 Darbaş, G., Gürbüz, K., 2017. Sedimentary evidence for late messinian
1238 uplift of the se margin of the central anatolian plateau: Adana basin,
1239 southern turkey. *Basin Research* 29, 488–514.
- 1240 Reid, M., Delph, J., Cosca, M., Schleiffarth, W., Gencalioglu Kuscü, G.,
1241 2019. Melt equilibration depths as sensors of lithospheric thickness during
1242 eurasia-arabia collision and the uplift of the anatolian plateau. *Geology*
1243 47, 943–947. URL: <https://doi.org/10.1130/G46420.1>, doi:10.1130/
1244 G46420.1.
- 1245 Reilinger, R., McClusky, S., Vernant, P., Lawrence, S., Ergintav, S., Cakmak,
1246 R., Ozener, H., Kadirov, F., Guliev, I., Stepanyan, R., Nadariya, M.,
1247 Hahubia, G., Mahmoud, S., Sakr, K., ArRajehi, A., Paradissis, D., Al-
1248 Aydrus, A., Prilepin, M., Guseva, T., Evren, E., Dmitrotsa, A., Filikov,
1249 S.V., Gomez, F., Al-Ghazzi, R., Karam, G., 2006. GPS constraints on
1250 continental deformation in the Africa-Arabia-Eurasia continental collision
1251 zone and implications for the dynamics of plate interactions. *Journal of*
1252 *Geophysical Research: Solid Earth* 111, 1–26. doi:10.1029/2005JB004051.

- 1253 Roman, C., 1973. Buffering plate: set of continental collision. *New Sci.* 57,
1254 830.
- 1255 Rosenbaum, G., Lister, G.S., Duboz, C., 2002. Relative mo-
1256 tions of africa, iberia and europe during alpine orogeny. *Tectono-*
1257 *physics* 359, 117–129. URL: [https://www.sciencedirect.com/](https://www.sciencedirect.com/science/article/pii/S0040195102004420)
1258 [science/article/pii/S0040195102004420](https://www.sciencedirect.com/science/article/pii/S0040195102004420), doi:[https://doi.org/10.](https://doi.org/10.1016/S0040-1951(02)00442-0)
1259 [1016/S0040-1951\(02\)00442-0](https://doi.org/10.1016/S0040-1951(02)00442-0).
- 1260 Rutherford, E., Burke, K., Lytwyn, J., 2001. Tectonic history of
1261 sumba island, indonesia, since the late cretaceous and its rapid es-
1262 cape into the forearc in the miocene. *Journal of Asian Earth*
1263 *Sciences* 19, 453–479. URL: [https://www.sciencedirect.com/](https://www.sciencedirect.com/science/article/pii/S1367912000000328)
1264 [science/article/pii/S1367912000000328](https://www.sciencedirect.com/science/article/pii/S1367912000000328), doi:[https://doi.org/10.](https://doi.org/10.1016/S1367-9120(00)00032-8)
1265 [1016/S1367-9120\(00\)00032-8](https://doi.org/10.1016/S1367-9120(00)00032-8).
- 1266 Sadeh, M., Hamiel, Y., Ziv, A., Bock, Y., Fang, P., Wdowinski, S., 2012.
1267 Crustal deformation along the Dead Sea Transform and the Carmel
1268 Fault inferred from 12 years of GPS measurements. *Journal of Geo-*
1269 *physical Research: Solid Earth* 117. URL: [https://doi.org/10.1029/](https://doi.org/10.1029/2012JB009241)
1270 [2012JB009241](https://doi.org/10.1029/2012JB009241), doi:<https://doi.org/10.1029/2012JB009241>.
- 1271 Şafak, Ü., Kelling, G., Gökçen, N.S., Gürbüz, K., 2005. The mid-cenozoic
1272 succession and evolution of the mut basin, southern turkey, and its regional
1273 significance. *Sedimentary Geology* 173, 121–150.
- 1274 Sançar, T., Zabcı, C., Karabacak, V., Yazıcı, M., Akyüz, H.S., 2019. Ge-
1275 ometry and Paleoseismology of the Malatya Fault (Malatya-Ovacık Fault
1276 Zone), Eastern Turkey: Implications for intraplate deformation of the Ana-
1277 tolian Scholle. *Journal of Seismology* 23, 319–340. URL: [https://doi.](https://doi.org/10.1007/s10950-018-9808-z)
1278 [org/10.1007/s10950-018-9808-z](https://doi.org/10.1007/s10950-018-9808-z), doi:[10.1007/s10950-018-9808-z](https://doi.org/10.1007/s10950-018-9808-z).
- 1279 Savage, J.C., Gan, W., Svarc, J.L., 2001. Strain accumulation and rotation in
1280 the eastern california shear zone. *Journal of Geophysical Research: Solid*
1281 *Earth* 106, 21995–22007. doi:<https://doi.org/10.1029/2000JB000127>.
- 1282 Schildgen, T.F., Cosentino, D., Bookhagen, B., Niedermann, S., Yildırım, C.,
1283 Echtler, H., Wittmann, H., Strecker, M.R., 2012. Multi-phased uplift of
1284 the southern margin of the central anatolian plateau, turkey: A record of

- 1285 tectonic and upper mantle processes. *Earth and Planetary Science Letters*
1286 317, 85–95.
- 1287 Schildgen, T.F., Yıldırım, C., Cosentino, D., Strecker, M.R., 2014. Linking
1288 slab break-off, hellenic trench retreat, and uplift of the central and eastern
1289 anatolian plateaus. *Earth-Science Reviews* 128, 147–168.
- 1290 Senel, M., 2002. 1:500000 scale geological maps of turkey, no:14 konya sheet.
1291 URL: www.mta.gov.tr.
- 1292 Sengör, A., 1979. The north anatolian transform fault: its age, offset and
1293 tectonic significance. *Journal of the Geological Society* 136, 269–282.
- 1294 Şengör, A., 1995. Sedimentation and tectonics of fossil rifts. *Tectonics of*
1295 *sedimentary basins* , 53–117.
- 1296 Şengör, A., Özeren, S., Genç, T., Zor, E., 2003. East anatolian high plateau as
1297 a mantle-supported, north-south shortened domal structure. *Geophysical*
1298 *Research Letters* 30.
- 1299 Şengör, A., Yalçın, N., Canitez, N., 1980. The origin of the adana/cilicia
1300 basin. an incompatibility structure arising at the common termination
1301 of the eastern anatolian and dead sea transform faults, in: *Sedimentary*
1302 *Basins of Mediterranean Margins*. C.N.R. Italian Project of Oceanography,
1303 pp. 45–46.
- 1304 Sengör, A.C., 1976. Collision of irregular continental margins: Implications
1305 for foreland deformation of alpine-type orogens. *Geology* 4, 779–782.
- 1306 Şengör, A.C., Özeren, M.S., Keskin, M., Sakıncı, M., Özbakır, A.D., Kayan,
1307 I., 2008. Eastern turkish high plateau as a small turkic-type orogen: Impli-
1308 cations for post-collisional crust-forming processes in turkic-type orogens.
1309 *Earth-Science Reviews* 90, 1–48.
- 1310 Şengör, A.C., Zabcı, C., Natal'in, B.A., 2019. Continental transform faults:
1311 congruence and incongruence with normal plate kinematics, in: *Transform*
1312 *plate boundaries and fracture zones*. Elsevier, pp. 169–247.
- 1313 Serpelloni, E., Vannucci, G., Anderlini, L., Bennett, R., 2016. Kinematics,
1314 seismotectonics and seismic potential of the eastern sector of the european

- 1315 alps from gps and seismic deformation data. *Tectonophysics* 688, 157–
1316 181. URL: [https://www.sciencedirect.com/science/article/pii/
1317 S0040195116303912](https://www.sciencedirect.com/science/article/pii/S0040195116303912), doi:[https://doi.org/10.1016/j.tecto.2016.09.
1318 026](https://doi.org/10.1016/j.tecto.2016.09.026).
- 1319 Seyitoğlu, G., Tunçel, E., Kaypak, B., Esat, K., Gökkaya, E., 2022. The
1320 anatolian diagonal: A broad left-lateral shear zone between the north ana-
1321 tolian fault zone and the aegean / cyprus arcs. *Türkiye Jeoloji Bülteni* 65,
1322 93 – 116. doi:10.25288/tjb.1015537.
- 1323 Sternai, P., Sue, C., Husson, L., Serpelloni, E., Becker, T.W., Wil-
1324 lett, S.D., Faccenna, C., Di Giulio, A., Spada, G., Jolivet, L., Valla,
1325 P., Petit, C., Nocquet, J.M., Walpersdorf, A., Castelltort, S., 2019.
1326 Present-day uplift of the european alps: Evaluating mechanisms and
1327 models of their relative contributions. *Earth-Science Reviews* 190,
1328 589–604. URL: [https://www.sciencedirect.com/science/article/
1329 pii/S0012825218304136](https://www.sciencedirect.com/science/article/pii/S0012825218304136), doi:[https://doi.org/10.1016/j.earscirev.
1330 2019.01.005](https://doi.org/10.1016/j.earscirev.2019.01.005).
- 1331 Tekeli, O., Aksay, A., Urdun, B.M., 1987. 1:100000 ölçekli acinsama nitelikli
1332 türkiye jeoloji haritaları serisi, kozan-j20 paftası.
- 1333 Ulu, U., 2002. 1:500000 scale geological maps of turkey, no: 15 adana sheet.
1334 URL: www.mta.gov.tr.
- 1335 Ulu, U., 2009. 1:100000 scale geological maps of turkey no:131, mersin o-33
1336 quadrangle.
- 1337 Van Buer, N.J., Jagoutz, O., Upadhyay, R., Guillong, M., 2015. Mid-crustal
1338 detachment beneath western tibet exhumed where conjugate karakoram
1339 and longmu–gozha co faults intersect. *Earth and Planetary Science Letters*
1340 413, 144–157.
- 1341 Viltres, R., Jónsson, S., Alouthman, A.O., Liu, S., Leroy, S., Masson, F.,
1342 Doubre, C., Reilinger, R., 2022. Present-day motion of the arabian plate.
1343 *Tectonics* 41, e2021TC007013. URL: [https://agupubs.onlinelibrary.
1344 wiley.com/doi/abs/10.1029/2021TC007013](https://agupubs.onlinelibrary.wiley.com/doi/abs/10.1029/2021TC007013), doi:[https://doi.org/10.
1345 1029/2021TC007013](https://doi.org/10.1029/2021TC007013).

- 1346 Walpersdorf, A., Pinget, L., Vernant, P., Sue, C., Deprez, A., the
1347 RENAG team, 2018. Does long-term gps in the western alps fi-
1348 nally confirm earthquake mechanisms? *Tectonics* 37, 3721–3737.
1349 URL: [https://agupubs.onlinelibrary.wiley.com/doi/abs/10.1029/](https://agupubs.onlinelibrary.wiley.com/doi/abs/10.1029/2018TC005054)
1350 [2018TC005054](https://doi.org/10.1029/2018TC005054), doi:<https://doi.org/10.1029/2018TC005054>.
- 1351 Wandrey, C., 2004. Sylhet-Kopili Barail-Tipam composite total petroleum
1352 system, Assam geologic province, India. *U.S. Geological Survey Bulletin*
1353 2208-D. URL: <http://pubs.usgs.gov/bul/b2208-d/>.
- 1354 Wang, K., Wells, R., Mazzotti, S., Hyndman, R.D., Sagiya, T., 2003.
1355 A revised dislocation model of interseismic deformation of the cascadia
1356 subduction zone. *Journal of Geophysical Research: Solid Earth* 108.
1357 URL: [https://agupubs.onlinelibrary.wiley.com/doi/abs/10.1029/](https://agupubs.onlinelibrary.wiley.com/doi/abs/10.1029/2001JB001227)
1358 [2001JB001227](https://doi.org/10.1029/2001JB001227), doi:<https://doi.org/10.1029/2001JB001227>.
- 1359 Wdowinski, S., Bock, Y., Baer, G., Prawirodirdjo, L., Bechor, N., Naa-
1360 man, S., Knafo, R., Forrai, Y., Melzer, Y., 2004. Gps measurements of
1361 current crustal movements along the dead sea fault. *Journal of Geophys-
1362 ical Research: Solid Earth* 109. URL: [https://agupubs.onlinelibrary.](https://agupubs.onlinelibrary.wiley.com/doi/abs/10.1029/2003JB002640)
1363 [wiley.com/doi/abs/10.1029/2003JB002640](https://doi.org/10.1029/2003JB002640), doi:[https://doi.org/10.](https://doi.org/10.1029/2003JB002640)
1364 [1029/2003JB002640](https://doi.org/10.1029/2003JB002640).
- 1365 Welford, J.K., Hall, J., Rahimi, A., Reiche, S., Hübscher, C., Louden,
1366 K., 2015. Crustal structure from the Hecataeus Rise to the Levan-
1367 tine Basin, eastern Mediterranean, from seismic refraction and gravity
1368 modelling. *Geophysical Journal International* 203, 2055–2069. URL:
1369 <https://doi.org/10.1093/gji/ggv422>, doi:[10.1093/gji/ggv422](https://doi.org/10.1093/gji/ggv422).
- 1370 Westaway, R., 2003. Kinematics of the middle east and eastern mediterranean
1371 updated. *Turkish Journal of Earth Sciences* 12, 5–46.
- 1372 Yetis, C., Demirkol, C., Lagap, H., Unlugenc, U.C., 1991. 1:100000 olcekli
1373 acinsama nitelikli turkiye jeoloji haritalari serisi, kozan-k20 paftasi.
- 1374 Zhao, L., Paul, A., Malusà, M.G., Xu, X., Zheng, T., Solarino, S., Guillot,
1375 S., Schwartz, S., Dumont, T., Salimbeni, S., Aubert, C., Pondrelli, S.,
1376 Wang, Q., Zhu, R., 2016. Continuity of the alpine slab unraveled by high-
1377 resolution p wave tomography. *Journal of Geophysical Research: Solid*
1378 *Earth* 121, 8720–8737. doi:<https://doi.org/10.1002/2016JB013310>.

- 1379 Özbey, V., Şengör, A.M.C., Özeren, M.S., 2022. Tectonics in
1380 a very slowly deforming region in an orogenic belt. *Tectono-*
1381 *physics* 827, 229272. URL: [https://www.sciencedirect.com/](https://www.sciencedirect.com/science/article/pii/S004019512200066X)
1382 [science/article/pii/S004019512200066X](https://www.sciencedirect.com/science/article/pii/S004019512200066X), doi:[https://doi.org/10.](https://doi.org/10.1016/j.tecto.2022.229272)
1383 [1016/j.tecto.2022.229272](https://doi.org/10.1016/j.tecto.2022.229272).
- 1384 Şengör, A.M.C., Görür, N., Şaroğlu, F., 1985. Strike-Slip Faulting
1385 and Related Basin Formation in Zones of Tectonic Escape: Turkey
1386 as a Case Study1. URL: <https://doi.org/10.2110/pec.85.37.0211>,
1387 doi:10.2110/pec.85.37.0211.
- 1388 Şengör, A.M.C., Lom, N., Sunal, G., Zabci, C., Sancar, T., 2019. The
1389 phanerozoic palaeotectonics of Turkey. Part I: an inventory. *Mediterranean Geoscience Reviews* 1, 91–161. URL: [https://doi.org/10.1007/](https://doi.org/10.1007/s42990-019-00007-3)
1390 [s42990-019-00007-3](https://doi.org/10.1007/s42990-019-00007-3), doi:10.1007/s42990-019-00007-3.
- 1392 Şengör, A.M.C., Zabci, C., 2019. The North Anatolian Fault and the
1393 North Anatolian Shear Zone BT , in: Kuzucuoglu, C., Çiner, A.,
1394 Kazanci, N. (Eds.), *Landscapes and Landforms of Turkey*. Springer In-
1395 *ternational Publishing, Cham*, pp. 481–494. URL: [https://doi.org/10.](https://doi.org/10.1007/978-3-030-03515-0-27)
1396 [1007/978-3-030-03515-0-27](https://doi.org/10.1007/978-3-030-03515-0-27), doi:10.1007/978-3-030-03515-0-27.
- 1397 Şengör, A.M. ; Stock, J., 2014. The ayyubid orogen: An ophiolite obduction-
1398 driven orogen in the late cretaceous of the neo-tethyan south margin. *Geo-*
1399 *science Canada* 41, 225–254.

1400 **Figure Captions**

Figure 1: Neotectonics of the Eastern Mediterranean region. Compressional structures denoted by blue lines, and extensional ones red. Those represented by the black lines are strike-slip faults. Tectonic structures were compiled from Tekeli et al. (1987); Ayhan (1988); Yetis et al. (1991); Ulu (2009); Dalkilic and Balci (2009); Bilgic (2009); Alan et al. (2011, 2012); Bilgin (2013); Alan et al. (2013); Şengör and Zabcı (2019, and cited studies therein). The structures around Adana-Cilicia Basins are taken from Aksu et al. (2005); Burton-Ferguson et al. (2005); Aksu et al. (2014a, 2021, and cited studies therein). The thick red arrows indicate the motion of giant plates and Anatolia schole. Thicker dashed blue rectangle points out the region of interest of this study.

Figure 2: Triple junctions located around the area. Red stars are the location of $M_w = 7.7$ and $M_w = 7.6$ Pazarcık and Elbistan earthquakes. Abbreviations: K=Kahramanmaraş triple junction, H=Hatay triple junction, ES=Eratosthenes seamount, CA=Cyprus arc, KR=Kyrenia range, Mr=Mersin, Bo=Bolkardağ, CB=Cilicia basin, AB=Adana basin, MB=Mut basin, GTP=Göksu-Taşeli plateau, CT-Me=Central Taurus Menderes block, Is=Iskenderun gulf, Go=Göksu river, C=Ceyhan river, S=Seyhan river

Figure 3: Incompatibility basins arising from triple junctions and their fate: A. Continent A and continent B are approaching at the expense of the intervening ocean, which is being consumed beneath continent A creating an easily deformable cushion at its margin. B. Continent B is divided into two pieces, B' and B'' by a north-south striking transform fault. When continent B'' collides with continent A's easily deformable cushion, it creates two strike-slip faults along which a portion of the easily deformable part of A is expelled westward. This leads to the formation of a Karhova-type incompatibility basin at a, and an Adana/Cilicia-type incompatibility basin at b. C. When full collision occurs following the elimination of all ocean between the two approaching continents, the previously formed incompatibility basins will also be squashed and obliterated out of recognition, except by careful local geological studies. If one is not consciously looking for them, they may be easy to miss amidst the complex structure of the ensuing collisional orogen and deprive the geologist of precious clues for the origin of some of the unexpected fabric encountered.

Figure 4: Geologic formations, digitized from (Ed. Senel, 2002, Geological Map of Turkey, Adana), (Ed. Ulu, 2002, Geological Map of Turkey, Konya), and Geological Survey Department of Cyprus (2009) younger than Oligocene and some formations were updated according to Öğretmen et al. (2018, fig. 2).

Figure 5: A. Menderes-Taurus Block after the Bozkır ophiolite obduction B. Menderes-Taurus block after the collision with the Kırşehir Massif along the Inner Tauride suture. M is the Menderes wing and B is the Bolkardağ wing. T is the 'belly of the Taurus'. The distribution of the Burdigalian deposits reveal the shape of the Mut Basin, a strike-slip related basin (uncertain whether a pull-apart or a constraining bend basin. We here prefer the latter. C. The geometry of the 'Mut type' strike-slip basin forming on a bulge of the hanging wall atop a thrust fault.

Figure 6: A. Rate of current uplift in the Central Alps. Notice that the maximum uplift coincides with the maximum thrust stacking under the Lepontine dome. B. Setting of the Cilicia/Adana Basin as a molasse basin in front of the impinging Tauride thrusts from the north. Notice that here too the maximum rate of uplift is atop the underthrusting of the maximum thickness of the continental lithosphere, despite the cold mantle under it. The lively seismicity shows that the thrusting of the Bolkardağ allochthon is still active albeit with a small rate of motion as judged from the small magnitude earthquakes. The Cilicia/Adana Basin is here shown as an equivalent of the Alpine molasse basin. The Kyrenia Range atop the Troodos/Paphos-Polis oceanic allochthon is an equivalent of the Jura mountains. The Seyhan and Ceyhan delta gradually fills the Cilicia/Adana basin from the eastern end just like the Shatt al-Arab delta in the Persian Gulf fills it from the north and the Ganges/Brahmaputra delta fills the Gulf of Bengal from the north. Further explanation is in the text

Figure 7: a) Unified Velocity field with respect to the Arabian fixed reference frame. Blue arrows represent the processed stations and red arrows show unified stations taken from previous studies. b) GPS sites around Cyprus and the southeastern coast of Turkey. Triangles show continuous sites and hexagons are survey mode sites. Each color represents different networks. c) Normalized and Weighted Root Mean Square histograms for the north and east components of the processed stations.

Figure 8: a) Block geometry and seismic activity around the region. Blue line represents the boundaries defined as dislocation sources, red lines, on the other hand, correspond to the other block boundaries which do not accumulate elastic strain. Focal mechanisms, derived from the Global Centroid Moment Tensor (Global CMT) catalog (Ekström and Nettles, 1997), represents the earthquakes bigger than $M_w = 4.5$ have occurred as of 1976. They were scaled according to their magnitudes. b) The cross sectional view from the northern tip of the Cyprus Arc to the Kyrenia range (yellow line on the map). Focal mechanisms and red dots, which are the earthquakes coincide with the domain of the cross section, were projected onto the section.

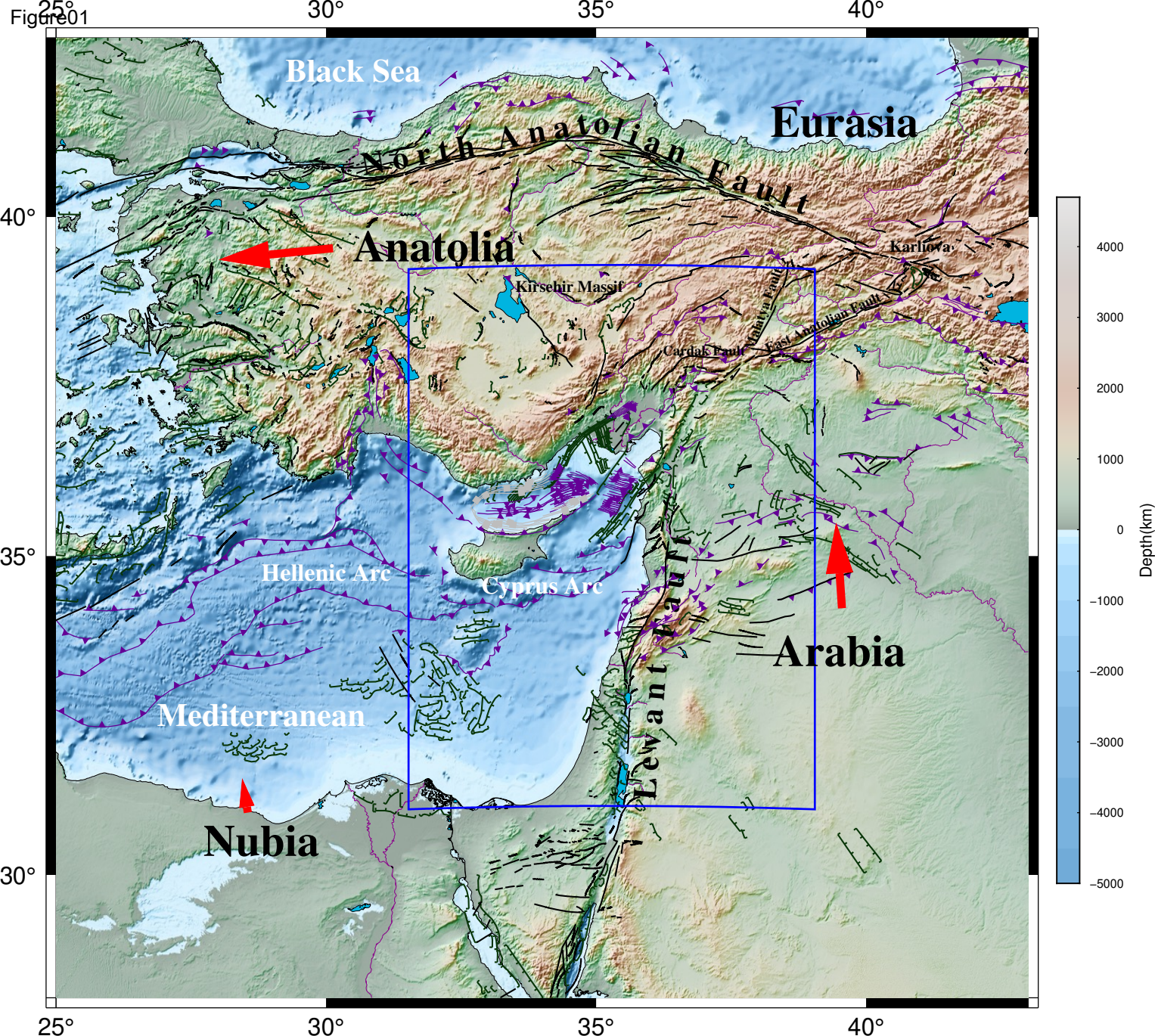
Figure 9: Checkerboard test. a-c are the forward of model coupling distribution of the test for low and high resolution patterns respectively. b-d shows the inversion results of these two tests.

Figure 10: Coupling coefficient distribution on the dislocation sources.

Figure 11: a) Fault slip rates and residual velocities. The values with no parentheses are the strike-slip rates (Positive means left lateral) and the slip rates within the parentheses are convergence rates (positive means compression). Red arrows are the strain rate crosses for each block. b) Cumulative histogram of the normalized residuals in Fig. 11a. The black curve indicates the chi-square distribution of the north and east components.

Figure 12: a) Strain rate field of the area. Arrow crosses are the principal strain rate tensor components. Black arrow belongs to the compression component of each tensor while white ones are the extensional component. The grid represents the areal strain change that accounts for the trace of the tensor for each cell. Grey color indicates the location out of the grid domain. b) Continuum Kinematic model solutions. Red arrows are the observed velocities and blue arrows are the model result.

Figure 13: Seismicity and the second invariant of the strain rate tensor (obeying the formula $\sqrt{\frac{1}{2}(\bar{\dot{\epsilon}}_{kl}\bar{\dot{\epsilon}}_{kl})}$). Grey color indicates the location out of the grid domain. Seismicity catalog was taken from Karabulut et al. (2019).



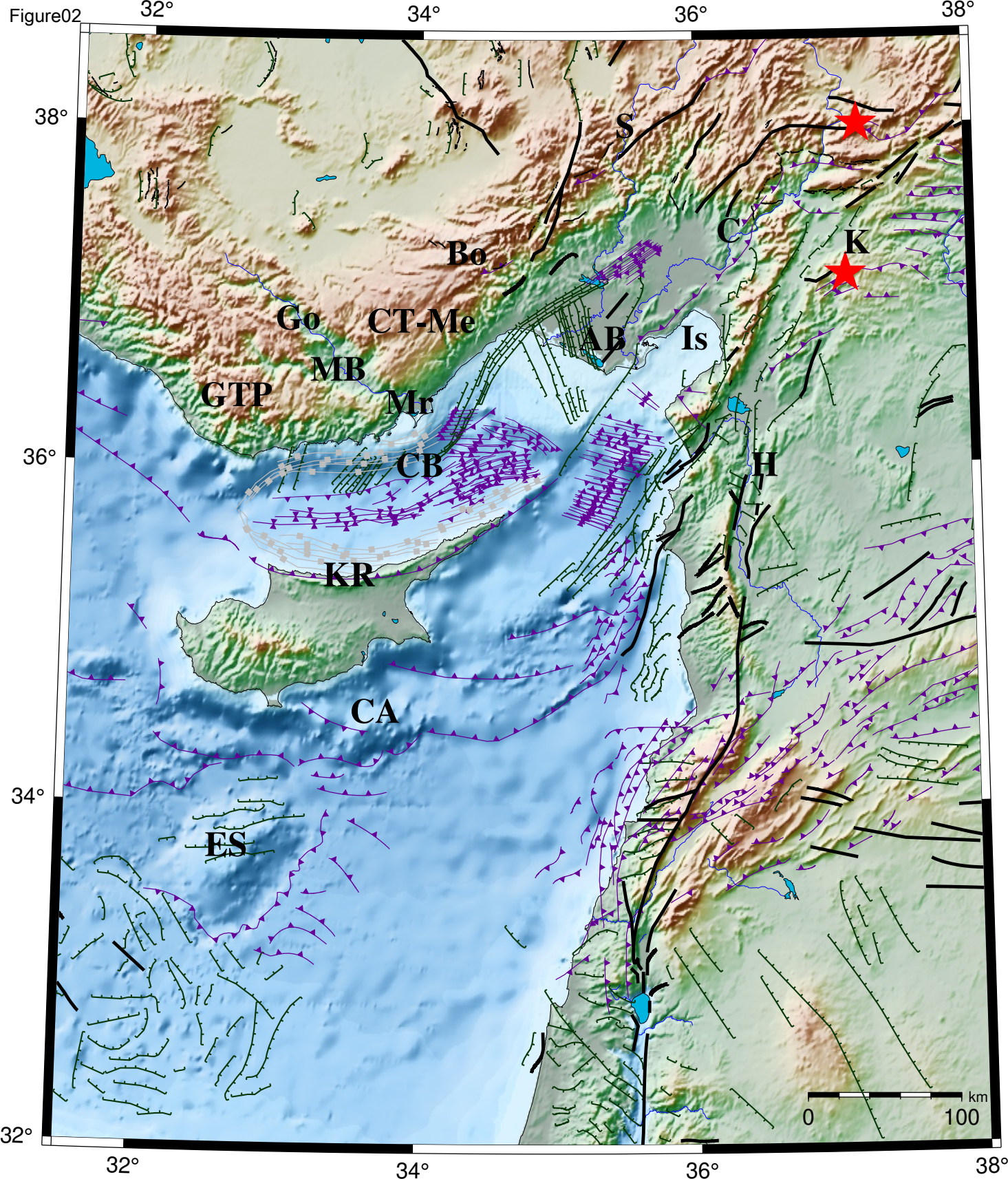


Figure03

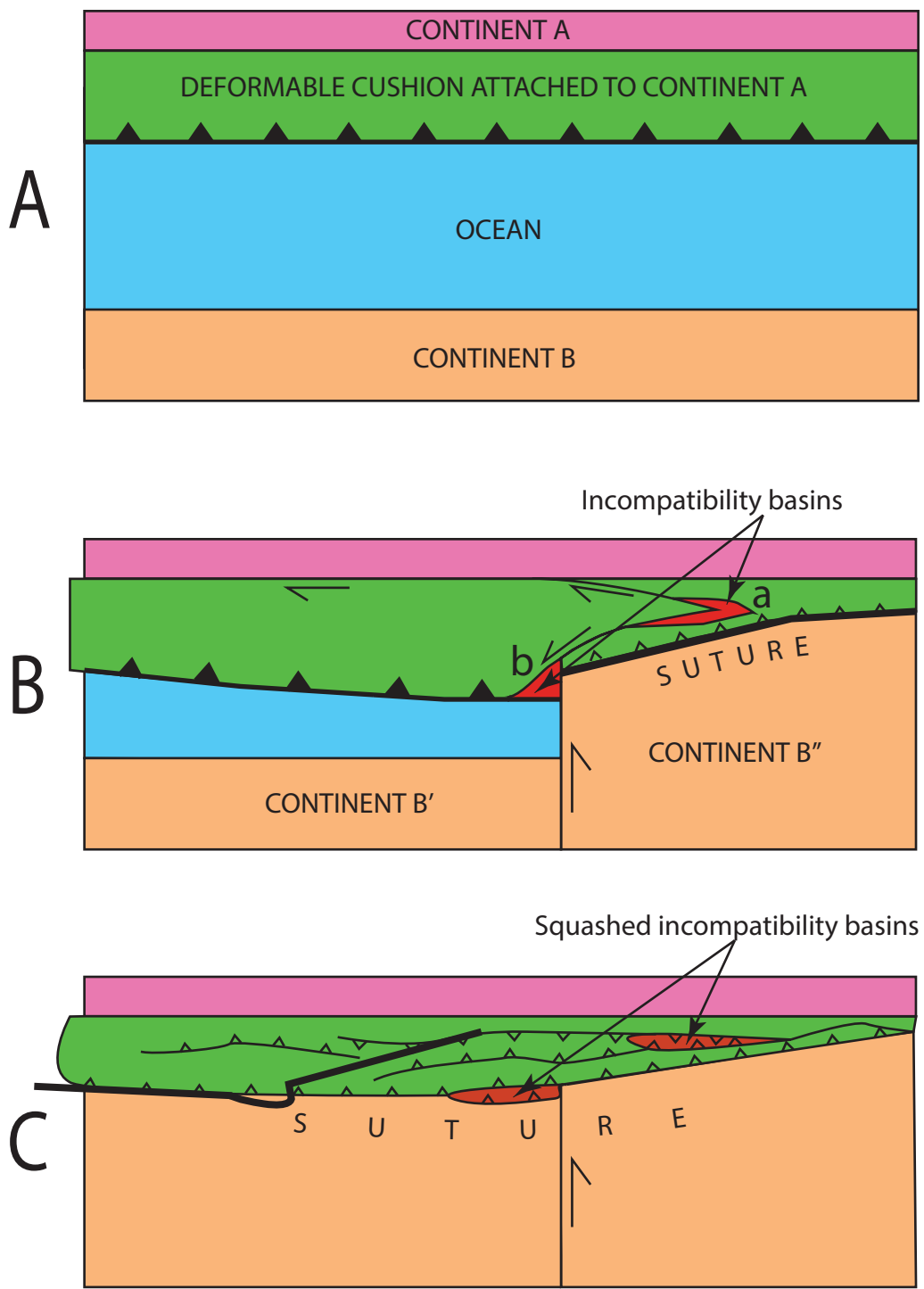
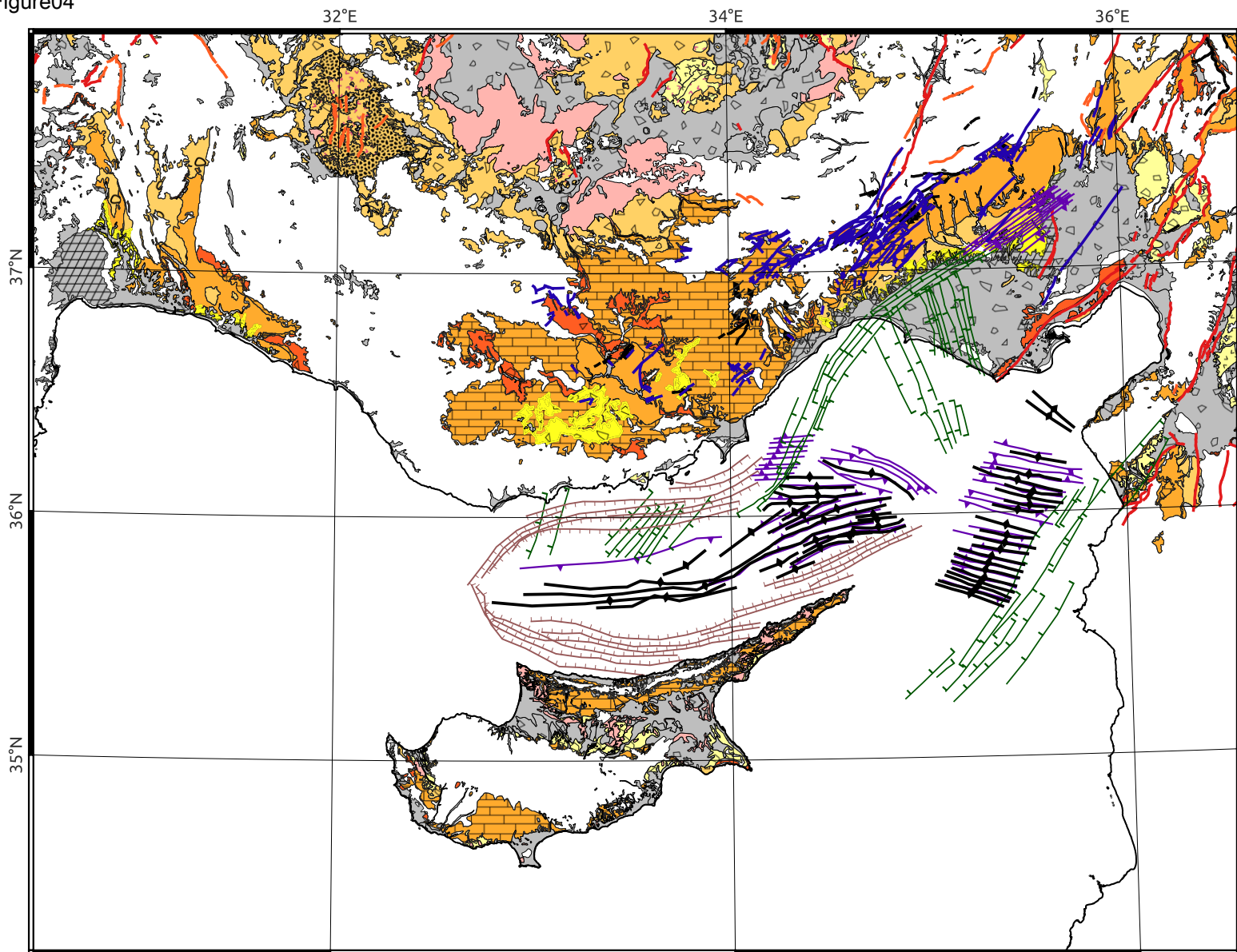


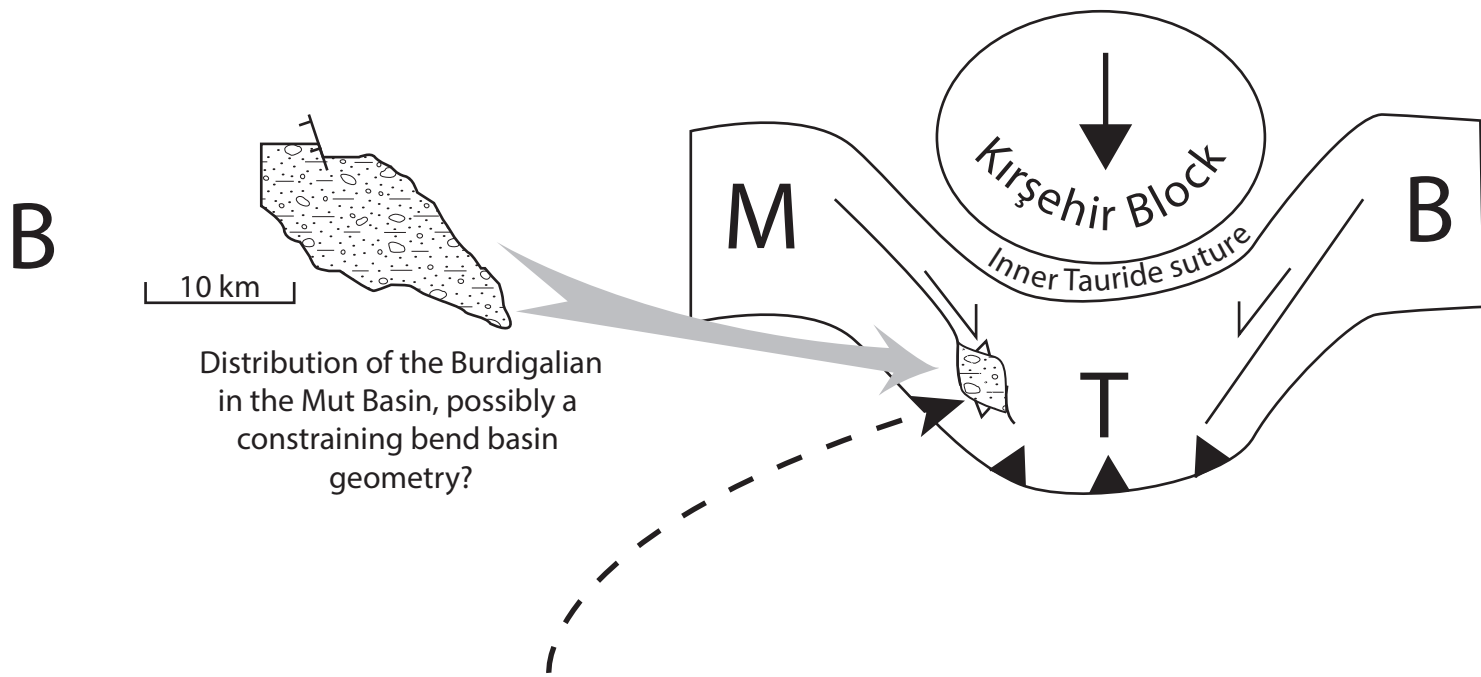
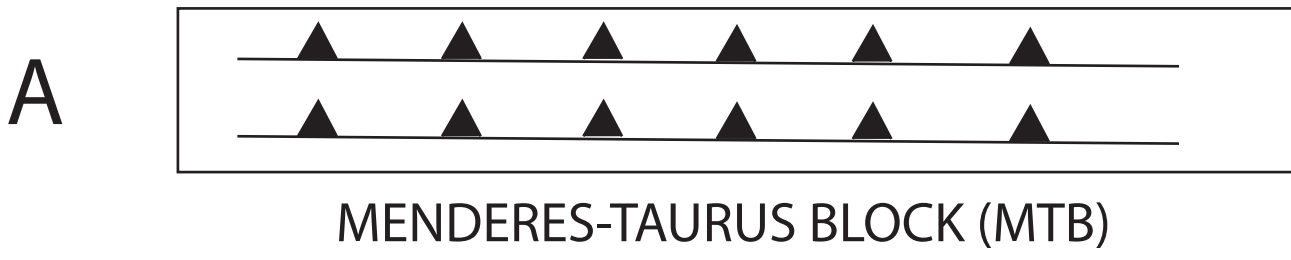
Figure04

**STRUCTURES**

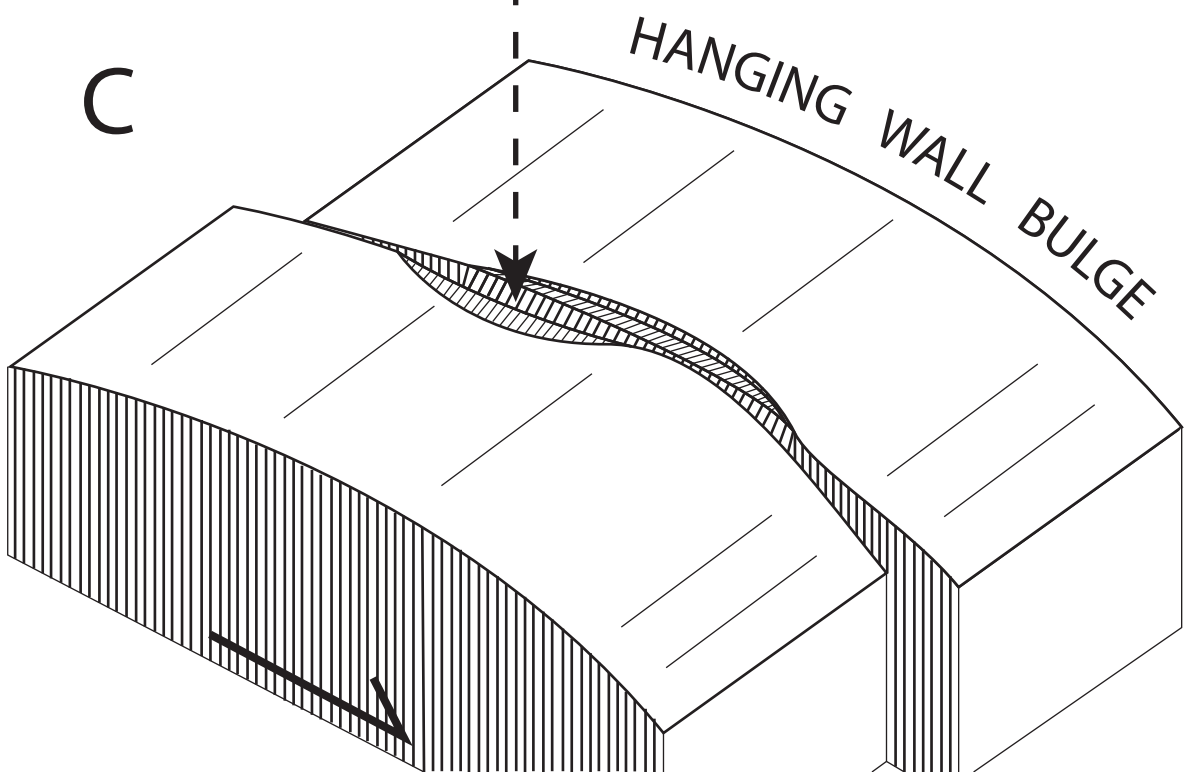
- Turkiye_Kiyi
- Probable_Quaternary_Faults_or_Lineaments
- ◆ Anticline
- Landslide
- Miocene_Faults
- ◆ Miocene_Folds
- Normal_Faults
- Thrust_Faults
- Holocene_Faults

GEOLOGY

- Quaternary_Alluvium
- Quaternary_Basalt
- Quaternary_Beach_Sands
- Quaternary_Pyroclastics
- Quaternary_Travertine
- Quaternary_Undifferentiated
- Pleistocene
- Pliocene_Andesite
- Pliocene_Basalt
- Pliocene_Pyroclastics
- Pliocene_Terrestrial_Clastics
- L_Pliocene_Terrestrial_Clastics
- L_Pliocene_Limestone
- U_Miocene_Andesite
- U_Miocene_Clastics
- U_Miocene_Pyroclastics
- U_Miocene_Sedimentary_Volcanics
- U_Miocene_Terrestrial_Clastics
- U_Miocene_Tortonian_Clastics
- M_Miocene_Basalt
- M_Miocene_Limestone
- M_Miocene_Clastics
- M_Miocene_Terrestrial_Clastics
- L_Miocene_Clastics
- L_Miocene_Limestone
- L_Miocene_Terrestrial_Clastics



Mut-type strike-slip basin (not further specified)



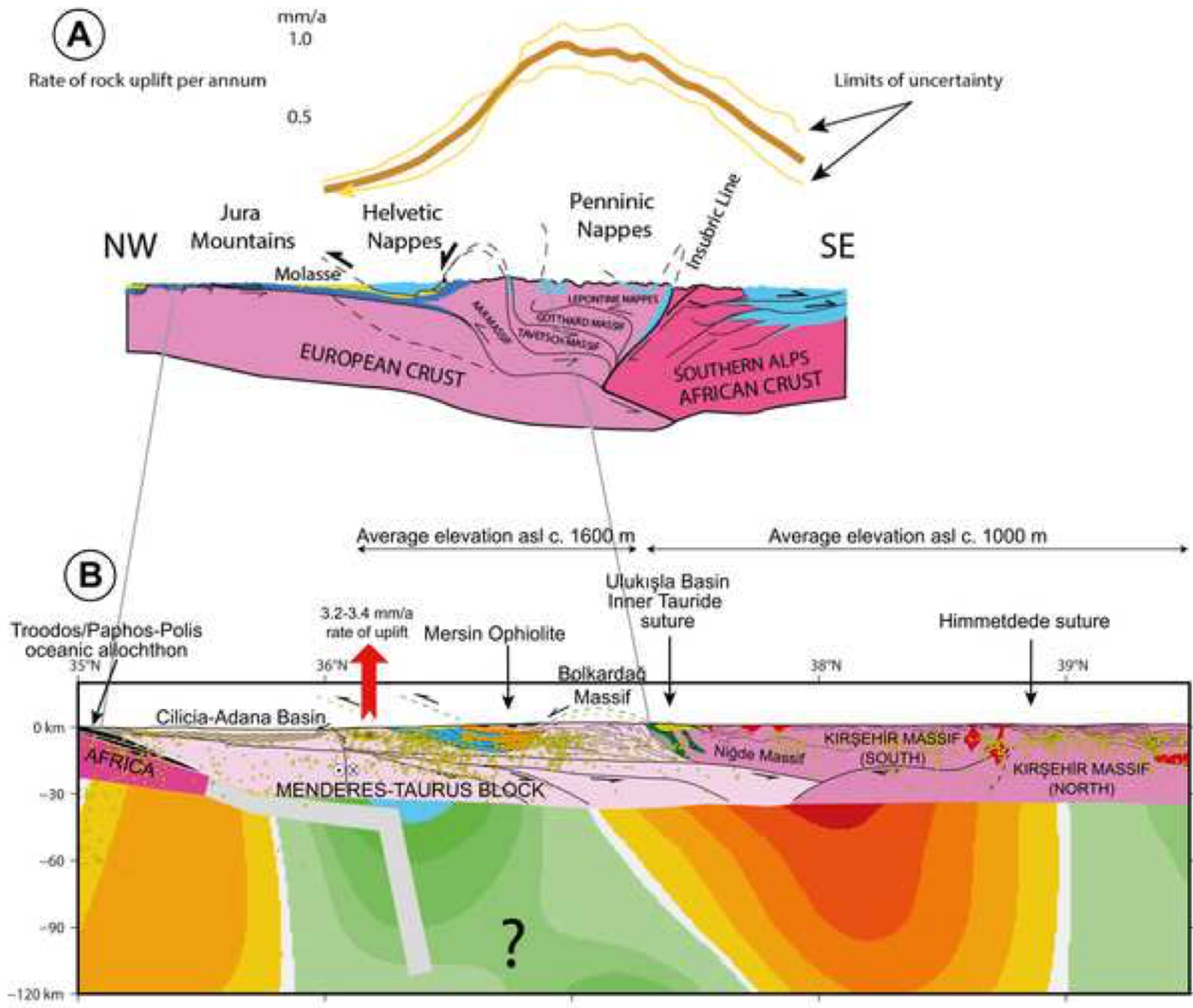


Figure 2

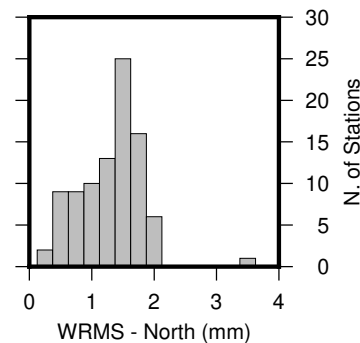
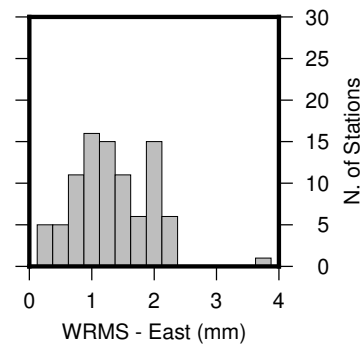
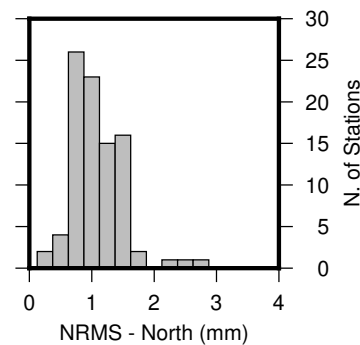
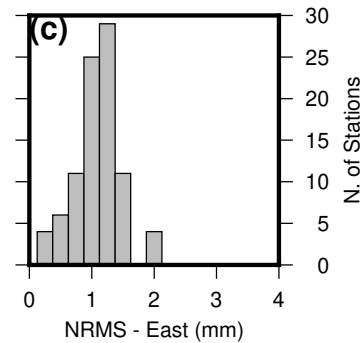
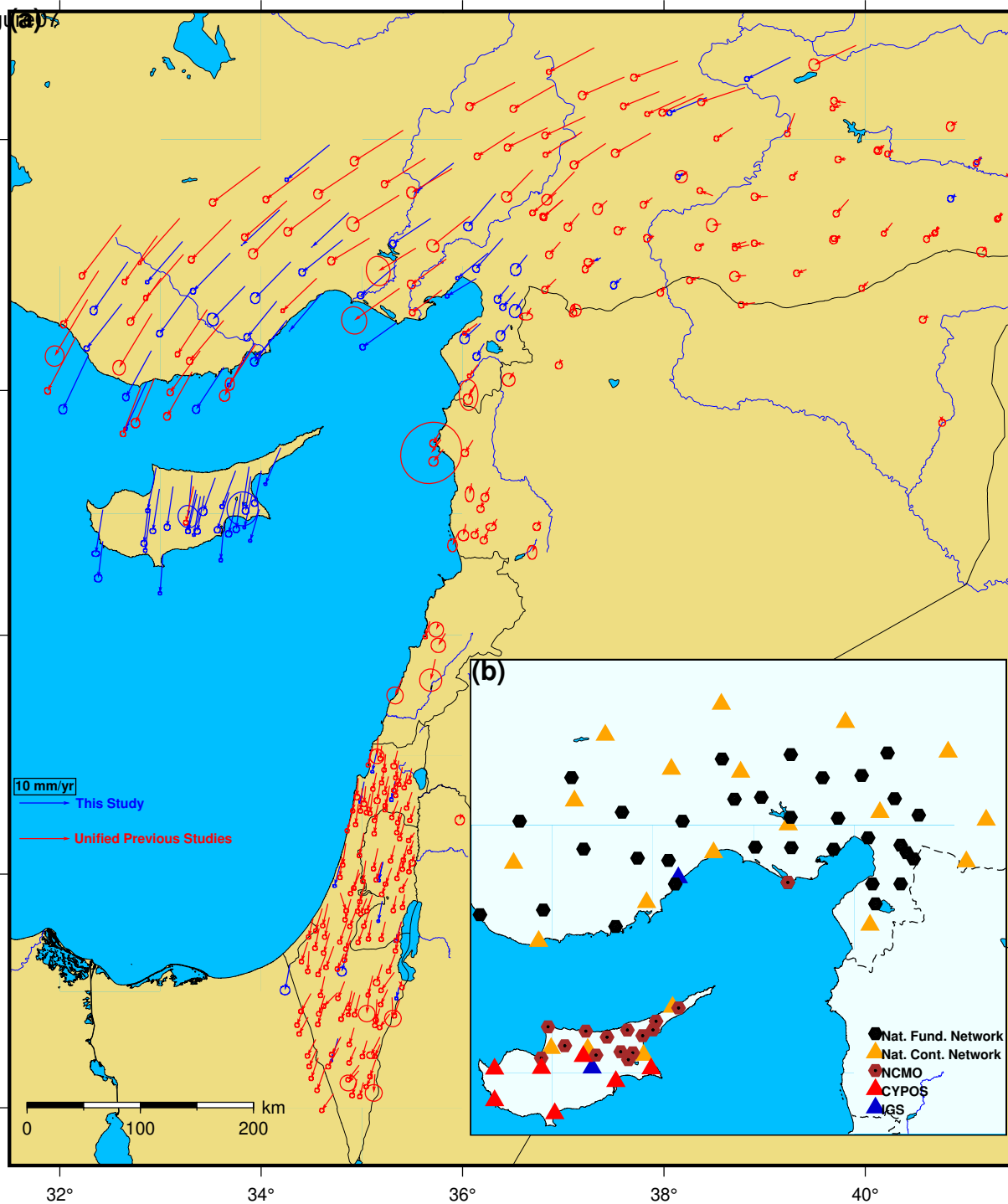


Fig. 108

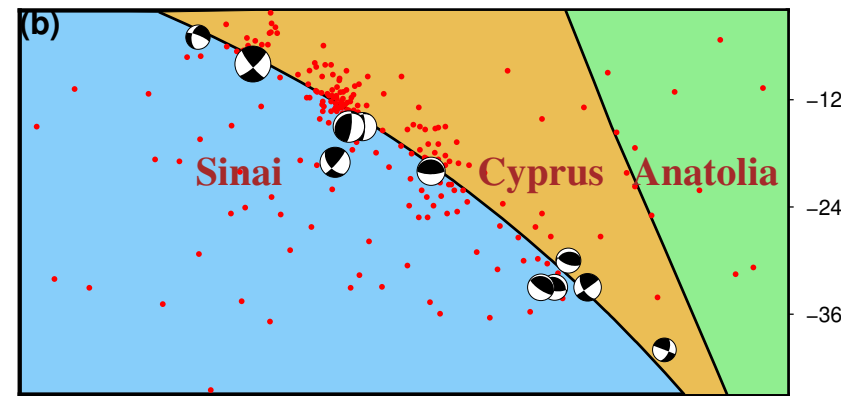
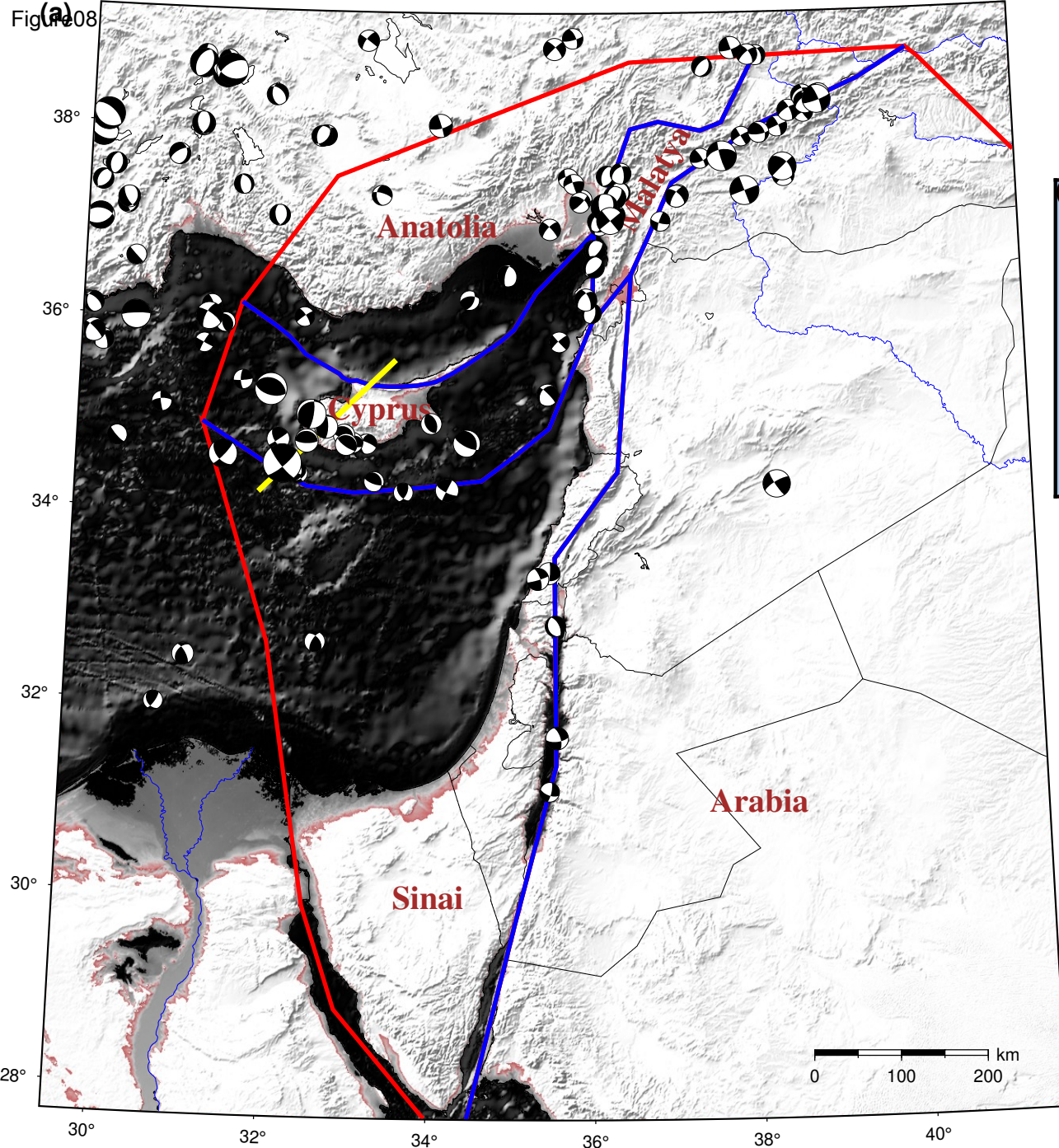


Figure 9

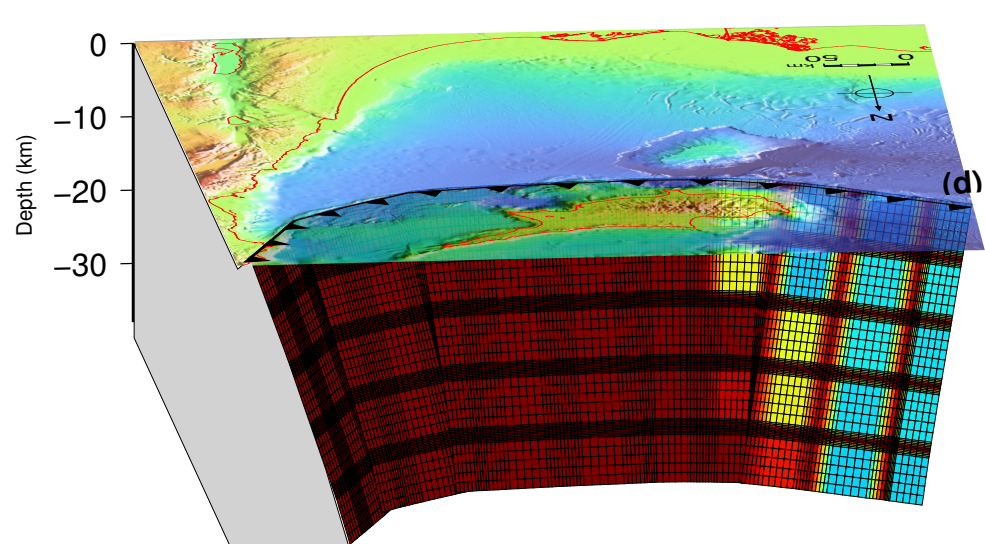
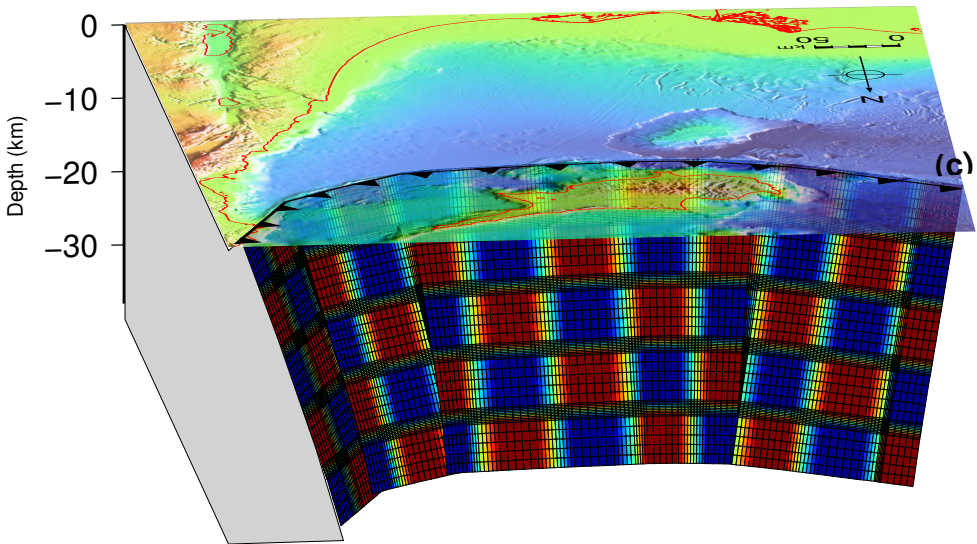
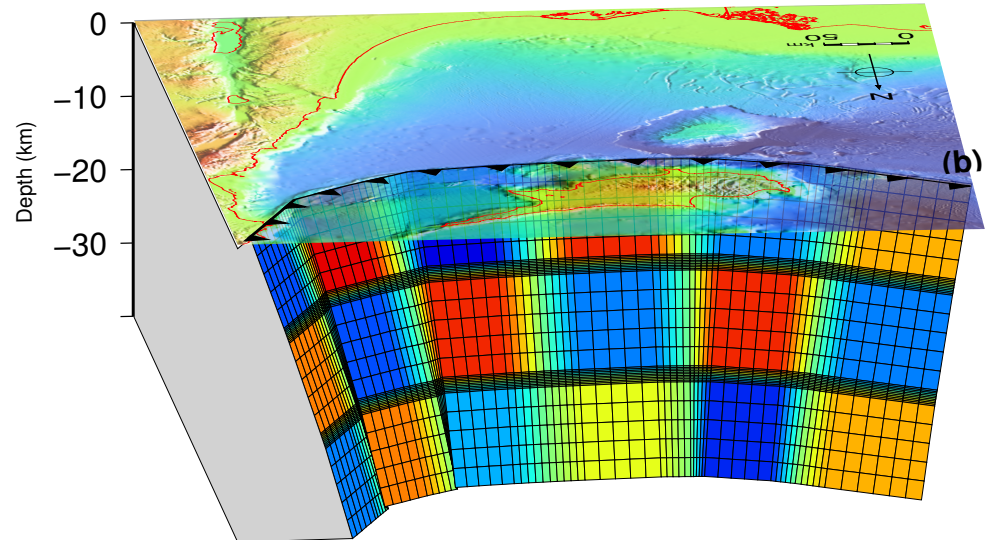
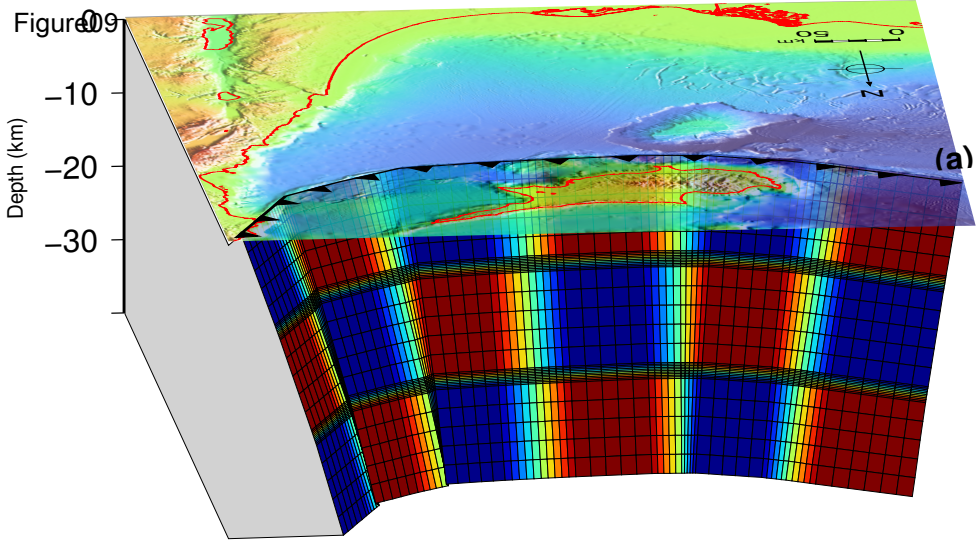
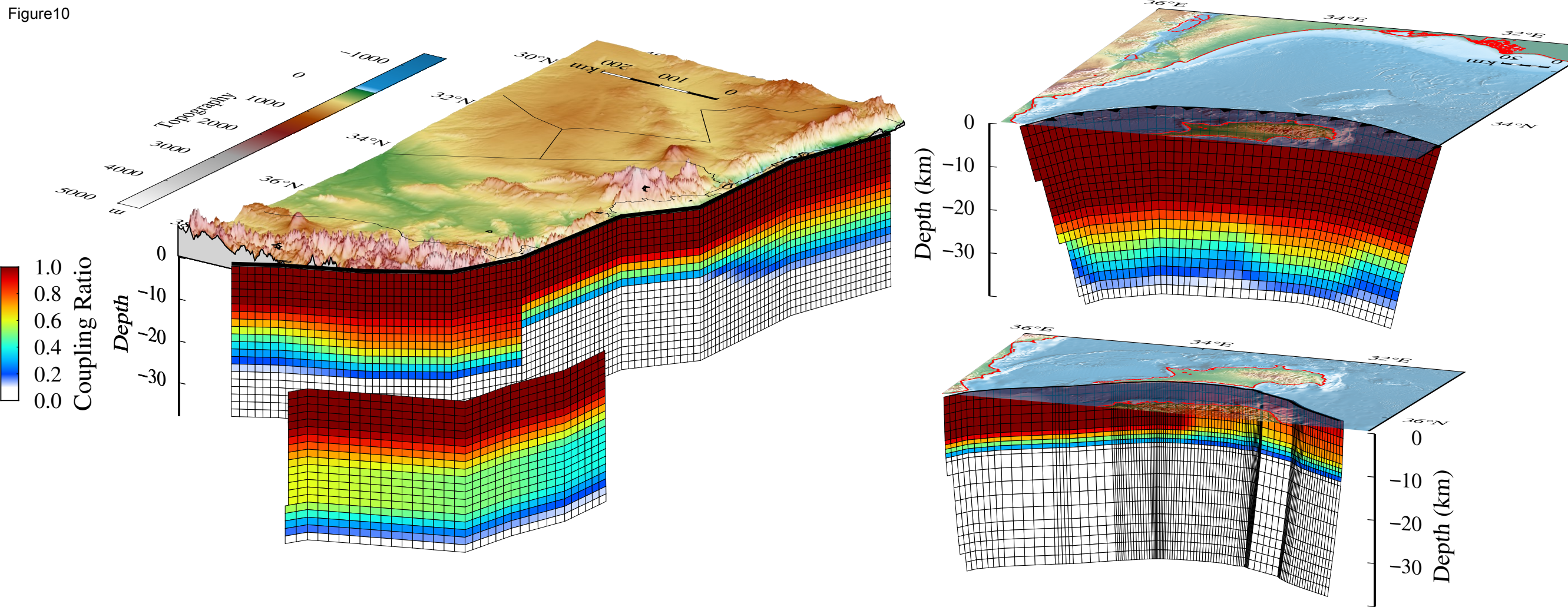


Figure10



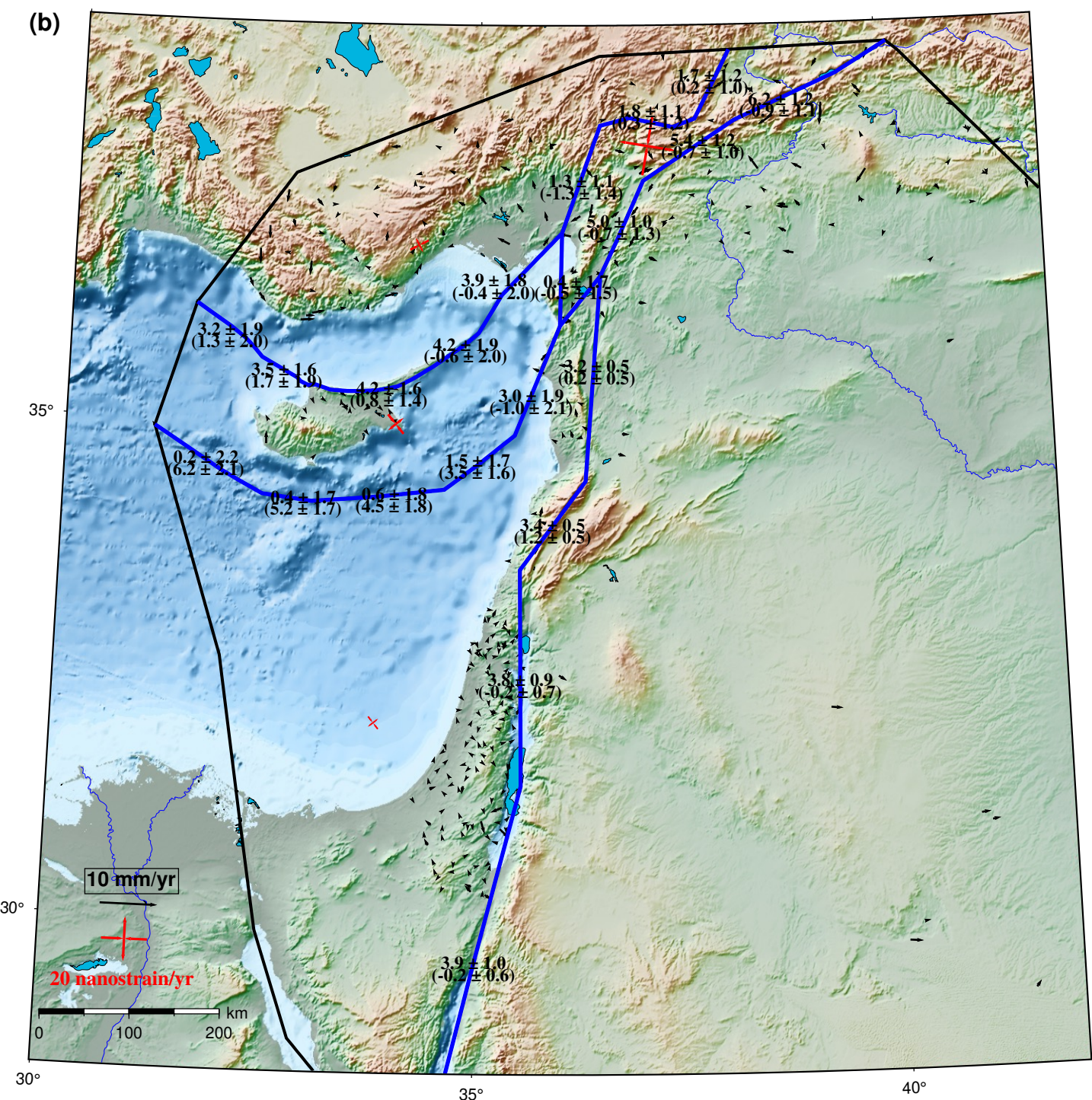
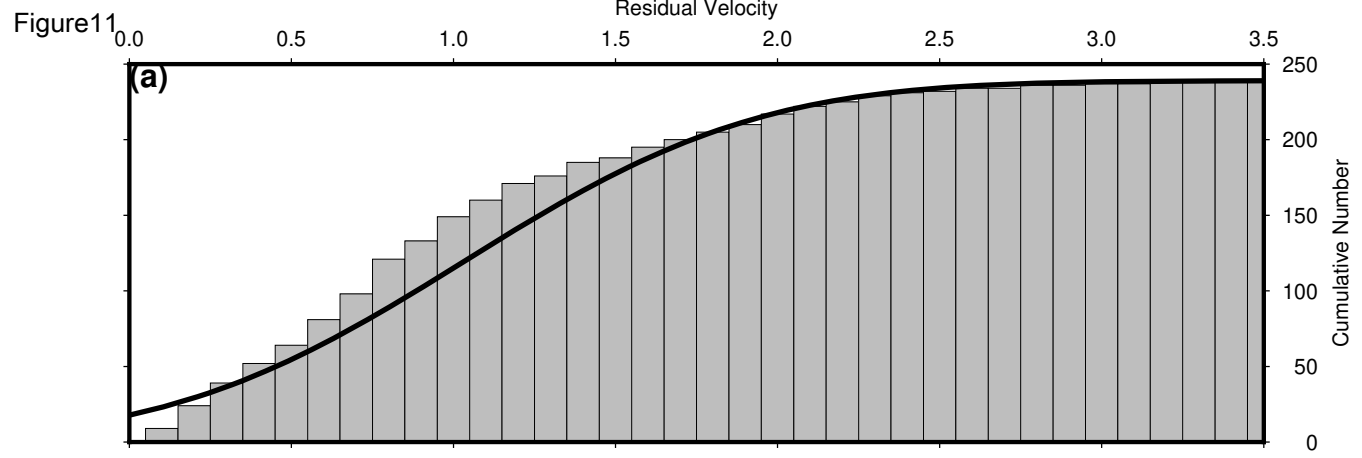
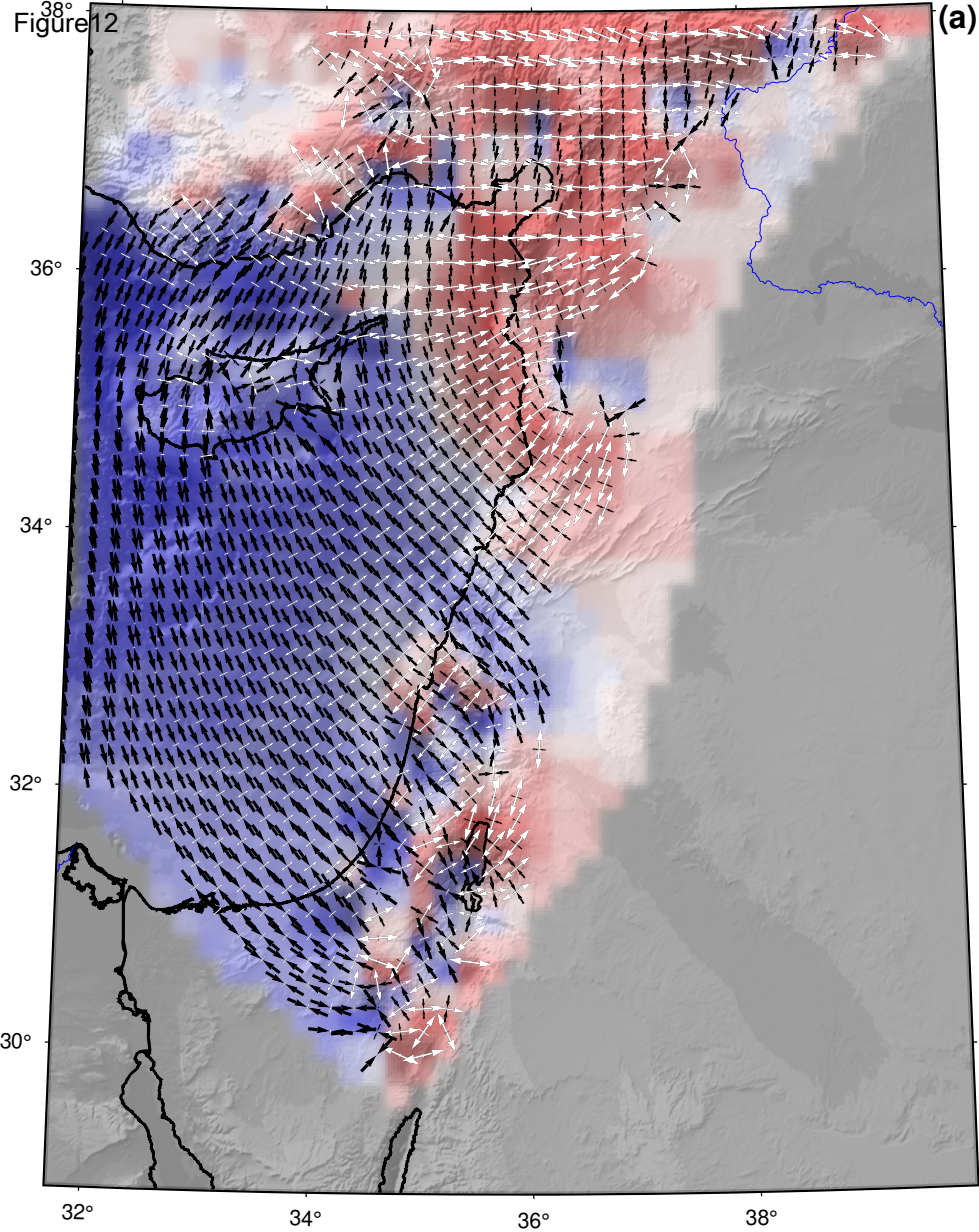


Figure 12



1st invariant (nanostrain/yr)

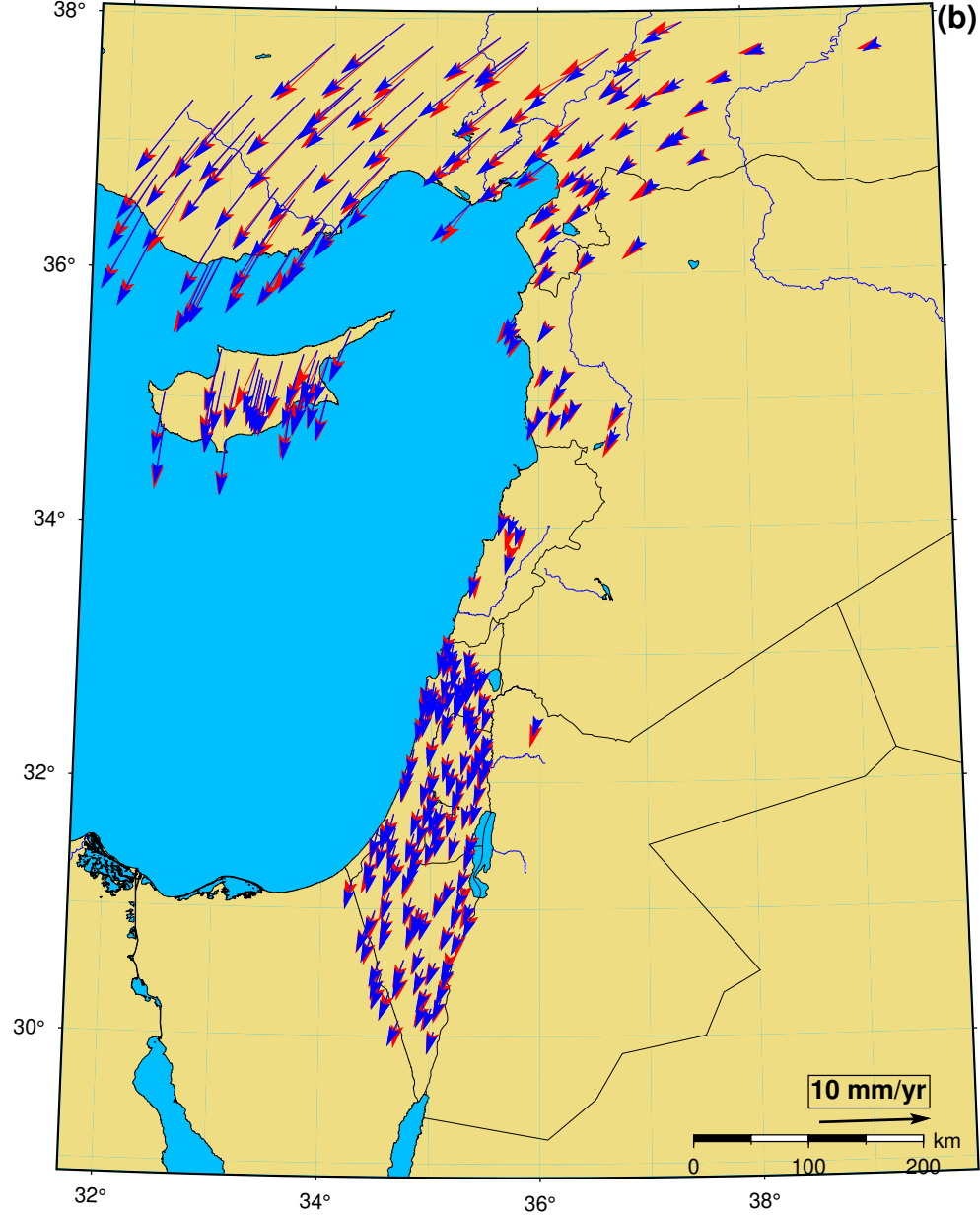
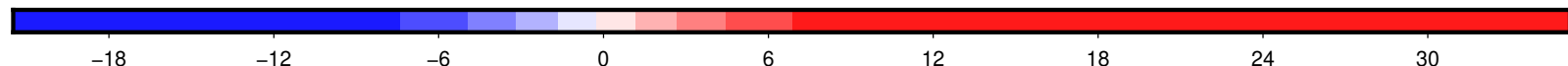
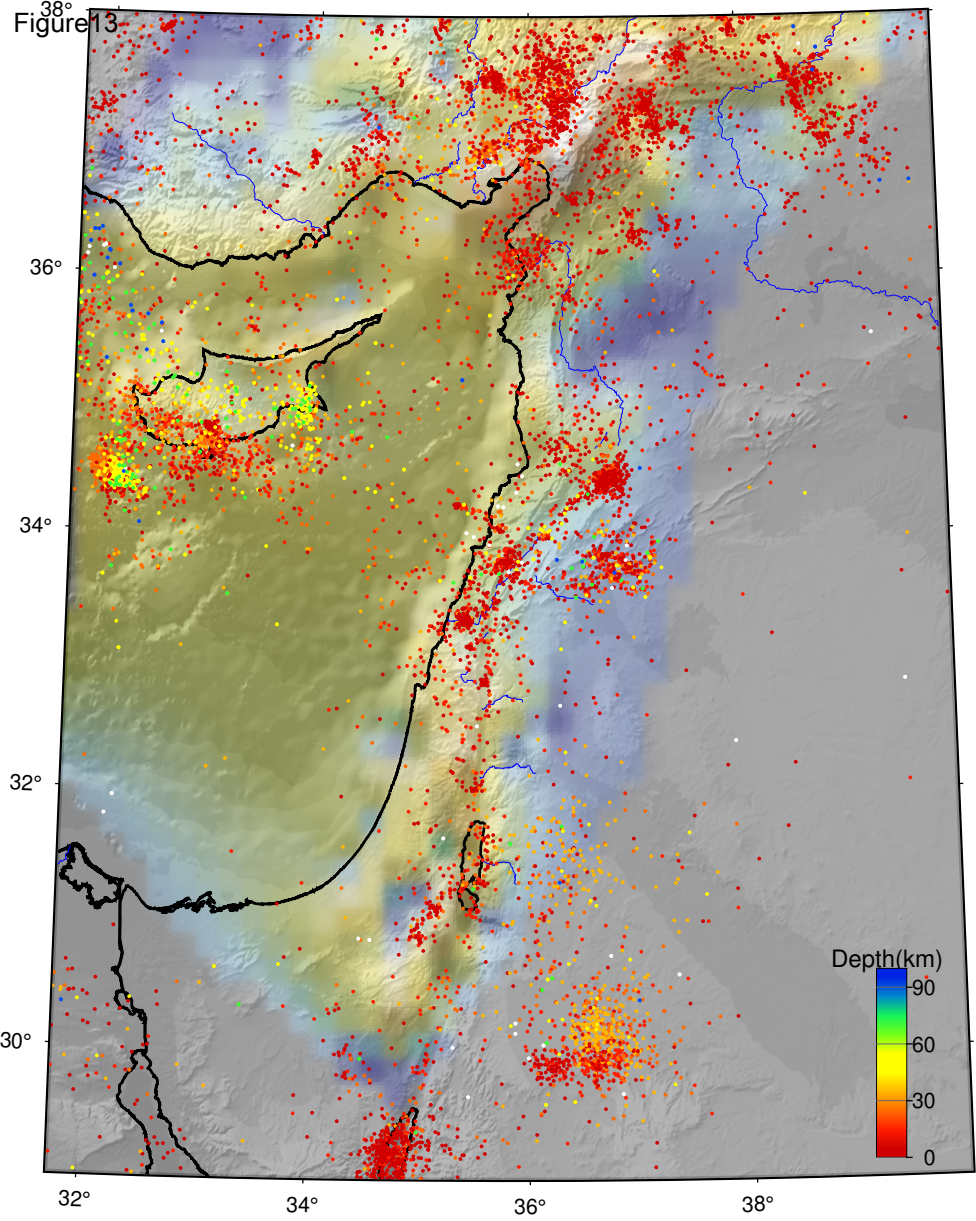


Figure 13



2nd invariant (nanostrain/yr)

